PERSIANN-Unet: A Global Deep Learning Framework for Near-Real-Time Precipitation Estimation Using Infrared Data

Phu Nguyen,[a] Vu Dao,[a] Tu Ung,[a] Claudia Jimenez Arellano,[a] Kuolin Hsu,[a] Soroosh Sorooshian,[a] Amir AghaKouchak, [a] George J. Huffman,[b] and F. Martin Ralph[c]

[a] *Center for Hydrometeorology and Remote Sensing (CHRS), Department of Civil and Environmental Engineering, University of California, Irvine, CA, USA*

[b] *NASA Goddard Space Flight Center, Greenbelt, Maryland*

[c] *Center for Western Weather and Water Extremes, Scripps Institution of Oceanography, University of California, San Diego, La Jolla, California*

Corresponding author: Phu Nguyen, ndphu@uci.edu

ABSTRACT

Access to high-quality, high-resolution, near-real-time precipitation data is essential for hydrological and meteorological research and disaster response. Traditional tools such as rain gauges and radar networks, though effective, are limited by sparse coverage in remote areas and radar constraints such as beam blockage and increasing beam height with range, which reduce near-surface accuracy. Satellite observations address these challenges by providing global coverage with fine spatial and temporal resolution. Many precipitation products combine geosynchronous thermal infrared (IR) and passive microwave (PMW) data. PMW sensors offer detailed atmospheric profiles but are restricted to infrequent overpasses and increasing reliance on smaller satellites with higher-frequency channels, which are less sensitive to liquid precipitation. In contrast, IR sensors provide consistent, high-frequency global observations, making them valuable for near-real-time estimation.

Recent advances in deep learning, particularly convolutional neural networks (CNNs), have further improved satellite precipitation retrievals. This study introduces PERSIANN-Unet (PUnet or PERSIANN V3), a quasi-global algorithm covering 60°N–60°S that combines IR data, monthly climatology, and the UNet architecture to produce half-hourly precipitation estimates at 0.04° resolution. The product is evaluated against HE, IMERG, and PDIR-Now for 2022–2023. Results show that PUnet closely matches its training target, IMERG V07 Final, at the global scale, and performance is further evaluated against Stage IV as a reference over CONUS. Training PUnet on IMERG (2016–2021) leverages a high-quality, integrated PMW-IR-gauge precipitation product while developing an IR-based framework not reliant on PMW availability. By operating on a single global image, PUnet avoids tile partitioning and blending steps, reducing edge discontinuities, and produces more spatially consistent precipitation fields across hemispheres.

SIGNIFICANCE STATEMENT

Reliable and timely precipitation data is critical for weather forecasting, flood monitoring, and climate research. However, traditional tools like rain gauges and radar systems are limited by sparse coverage in remote or data-scarce regions and require substantial infrastructure. This study presents PERSIANN-Unet (PUnet or PERSIANN V3), a quasi-global (60°S–60°N) precipitation estimation model that leverages deep learning with satellite infrared imagery and monthly climatology to generate near-real-time rainfall estimates at 0.04° and 30-min resolution. Compared to existing satellite products, PUnet shows closer agreement with IMERG Final across global and regional domains. Its global architecture provides a consistent and scalable framework for near-real-time precipitation estimation and long-term climate data record development.

1. Introduction

Access to high-quality, high-resolution, near-real-time precipitation data is crucial for the hydrological and meteorological communities. This data is key for studying events such as droughts, floods, or tropical cyclones, and can be extremely useful for disaster mitigation. The most-used tools to measure precipitation are rainfall gauges (AghaKouchak and Nkhjiri 2012; Sarojini et al. 2016). Although rain gauges provide in situ precipitation measurements, they represent point-scale observations available only at the gauge location and can be sparse in remote areas and mountainous regions. As a result, deriving a spatially continuous precipitation field requires interpolation or areal averaging of these discrete measurements, which introduces additional uncertainty, particularly in data-sparse regions and complex terrain (Sarojini et al. 2016; Sun et al. 2018). Radar networks are also commonly utilized to estimate precipitation (Zhang et al. 2016). Despite providing high-resolution estimates, ground-based radar observations can be affected by beam blockage in mountainous areas, and radar beam height increases with range, making measurements progressively less representative of near-surface precipitation, particularly near and above the freezing level (Seo et al. 2000). In addition, radar coverage is uneven at the global scale: while dense networks exist over parts of North America, Europe, and East Asia, many regions such as Africa, South America, and most of the world's

oceans have limited or no radar observations. Satellite data is a source of near-real-time precipitation estimates with high spatial and temporal resolutions (Faridzad et al. 2018). One strong advantage is that it is available globally, even in areas where in-situ measurements are nonexistent (Faridzad et al. 2018). Satellites provide an indirect estimate of precipitation through a relationship between the rainfall rate and the electromagnetic signal measured by the sensors (Nguyen et al. 2020).

There are two main types of satellite data used for precipitation estimation: passive microwave (PMW) and geosynchronous thermal infrared (IR) data. PMW sensors onboard Low Earth Orbiting (LEO) satellites collect information on the vertical profile of atmospheric temperature and humidity, and the liquid and frozen hydrometeors in clouds (Joyce et al. 2004; Miller et al. 2001; Sorooshian et al. 2002). However, PMW sensors are limited by the relatively narrow instantaneous swath of each overpass, requiring multi-satellite constellations to achieve adequate temporal sampling for monitoring global precipitation at short timescales. In contrast, IR observations from Geostationary Earth Orbit (GEO) satellites provide frequent imagery (typically every 5–30 minutes) at ~2–4 km spatial resolution. In addition to IR, visible (VIS) channels provide complementary information on cloud optical properties and structure. Recent studies have shown that combining VIS and IR can improve precipitation retrieval accuracy relative to IR-only approaches (Pfreundschuh et al. 2022a, 2025). It is worth noting that IR sensors are only able to collect information from the top of the clouds instead of penetrating the clouds and directly sensing hydrometeors like PMW sensors do (Grecu et al. 2004). Nevertheless, the high sampling frequency of IR makes it is an attractive candidate for estimating precipitation.

Satellite precipitation products that leverage the use of IR and/or PMW data have been developed for decades. An early example is the Precipitation Estimation from Remotely Sensed Information using Artificial Neural Networks (PERSIANN) algorithm, introduced by Hsu et al. (1997) at the Center for Hydrometeorology and Remote Sensing (CHRS) at the University of California, Irvine (UCI). PERSIANN estimates rainfall rates primarily from geostationary infrared imagery, and has since expanded into a family of products spanning near-real-time applications and long-term climate data records. The latest near-real-time PERSIANN product is called PERSIANN-Dynamic Infrared Rain Rate near-real-time (PDIR-Now), provides hourly

quasi-global IR-based precipitation estimates (Nguyen et al. 2020). More recently, other groups have advanced neural-network and deep-learning retrievals, particularly for PMW sensors. Examples include the Passive Microwave Neural Network Precipitation Retrieval (PNPR) algorithm developed for the conical-scanning Global Microwave Imager (GMI) radiometer (Sano et al. 2018) and GPROF-NN, a neural-network implementation of the Goddard Profiling algorithm (Pfreundschuh et al. 2022b). Another approach is to combine IR observations with physically based PMW retrievals, which is applied by the Integrated Multi-satellitE Retrievals for Global Precipitation Measurement (IMERG, Huffman et al. 2020). The National Oceanic and Atmospheric Administration (NOAA) Climate Prediction Center (CPC) MORPHing (CMORPH) algorithm is another example of a precipitation product that uses both PMW and IR data in its estimates (Joyce and Xie 2004).

Machine learning has become an increasingly important tool for precipitation estimation, enabling deep learning models to learn from vast datasets and produce results closely aligned with the data on which they were trained. Convolutional Neural Networks (CNNs), in particular, have proven effective for this purpose. For example, Sadeghi et al. (2020) employed a UNet-based CNN combined with geographical information to enhance the accuracy of precipitation retrieval algorithms. Similarly, CNNs have been applied to improve precipitation estimation in numerical weather prediction models (Pan et al. 2019). Additionally, Gorooh et al. (2022) developed Deep-STEP, a deep CNN algorithm designed to estimate precipitation using both PMW and IR data. This model utilizes PMW brightness temperatures at emission and scattering frequencies, along with IR brightness temperature and surface information, to extract cloud features. Furthermore, Chen et al. (2020) introduced a multi-layer perceptron (MLP) machine learning model to estimate precipitation, using IR and PMW as inputs and radar data as the target.

A major limitation in existing machine learning algorithms is that they are trained and applied on tiled images, each representing a small fraction of the globe; when non-overlapping or naively tiled approaches are used, this can lead to edge artifacts and inconsistencies when tiles are stitched together for global applications. Blended tiling strategies provide an effective alternative by employing overlapping tiles combined through spatial weighting functions, substantially reducing tile-boundary artifacts and enabling high-resolution retrievals, as

demonstrated in several recent global and regional retrieval frameworks (Amell et al. 2024; Pfreundschuh et al. 2025). In contrast to tile-based methods, the present study utilizes a single image of the entire globe. By avoiding tiled inference altogether, the model eliminates seam artifacts and can learn precipitation patterns across both the Northern and Southern hemispheres simultaneously. This single-image approach represents a complementary design choice that prioritizes global spatial coherence and methodological simplicity, at the expense of requiring downsampling to a coarser spatial resolution. Merged PMW–IR products like IMERG provide state-of-the-art precipitation estimates but rely heavily on high-quality PMW observations, whose future information content may be limited by shifts toward smaller satellite platforms. In contrast, geostationary IR observations remain globally available with stable quality. Motivated by this, we develop PERSIANN-Unet (hereafter, PUnet), a global deep-learning model that leverages IR data and monthly climatology. Trained against IMERG over 2016–2021, a period with the most complete IR record and stable GPM/IMERG processing, PUnet combines the accuracy of IMERG's high-quality merged PMW-IR-gauge retrievals with the operational stability of IR observations. This operational data product aims to provide precipitation estimates with a half-hourly temporal resolution and a spatial resolution of 0.04° x 0.04°, delivering a comprehensive and high-resolution view of global precipitation patterns with minimal latency. The PUnet global estimates are evaluated against established products, including HE, IMERG Final, and PDIR-Now, to assess the performance of the newly developed model across various temporal and spatial scales. IMERG Final and Stage IV serve as the benchmark dataset and references for evaluating the PUnet model, enabling quantitative assessment of the new IR precipitation estimation scheme. Although other near-real-time satellite precipitation products, such as CMORPH, GSMaP, and IMERG Early, provide reliable global precipitation estimates, only HE and PDIR-Now are selected for comparison. This comparison with IR-only satellite products is provided for context because these algorithms share similar IR-only inputs; however, it is not fully independent because PUnet is trained on IMERG and IR-only products such as PDIR are ingested into IMERG. Independent evaluation is therefore emphasized using ground-based reference datasets, including Stage IV over CONUS.

2. Data

143 Table 1 summarizes all datasets used in the study. More details are provided in the following
144 sections.

145 **Table 1**. Summary of all datasets used in this study.

Dataset	Role	Data Type	Spatial Resolution	Temporal Resolution	Units	Coverage	Data Period	Source
IR Data	Input	CPC geosynchronous satellite IR brightness temperature	0.04° × 0.04°	Half-hourly	K	Quasi-global (60°S–60°N)	2000–present	NOAA (Janowiak et al. 2001)
WorldClim 2 Precipitation	Input	Gauge-based interpolated climatological precipitation	0.01° × 0.01°	Monthly climatology	mm	Global land	1970–2000	WorldClim2 (Fick & Hijmans 2017)
PERSIANN-CDR	Input	Geosynchronous satellite IR-based precipitation	0.25° × 0.25°	Daily, Monthly	mm	Quasi-global (60°S–60°N)	1983–present	CHRS, UCI (Ashouri et al. 2015)
IMERG V07 Final (IMERGF)	Target/ Evaluation	Merged PMW–IR–gauge precipitation	0.1° × 0.1°	Half-hourly	mm/h	Global (90°S–90°N)	1998–present	NASA GPM (Huffman et al. 2023b)
PDIR-Now	Evaluation	Geosynchronous satellite IR-based precipitation	0.04° × 0.04°	Hourly, 6-hourly, daily	mm	Quasi-global (60°S–60°N)	2000–present	CHRS, UCI (Nguyen et al. 2019, 2020)
Hydro Estimator (HE)	Evaluation	Geosynchronous satellite IR-based precipitation	0.04° × 0.04°	Hourly, 6-hourly, daily	mm	Quasi-global (60°S–60°N)	2002–present	NOAA GOES (Scofield and Kuligowski 2003)
NCEP Stage IV (ST4)	Evaluation	Ground-based radar precipitation product	0.04° × 0.04°	Hourly, 6-hourly, daily	mm	CONUS	2002–present	NCEP (Lin et al. 2005; Du 2011)
PUnet	Model developed in this study	Deep learning IR-based precipitation	0.04° × 0.04°	Hourly, 6-hourly, daily	mm	Quasi-global (60°S–60°N)	2000–present	This study

146 *a. Input Data*

147 1) NOAA CLIMATE PREDICTION CENTER 4 KM (CPC-4KM) IR DATA

The CPC-4km IR dataset combines 11-micrometer brightness temperature (Tb) data from various geostationary satellites, including Himawari-8, GOES-E, GOES-W, Meteosat-11, and Meteosat-9 (Huffman et al. 2023). The merging process results in a unified half-hourly infrared Tb field at a spatial resolution of 4 kilometers (Janowiak et al. 2001). This dataset is computed by CPC. IR data is one of the primary inputs for generating PUnet precipitation estimates. The CPC-4km IR dataset is publicly available through NASA Goddard Earth Sciences Data and Information Services Center (GES DISC) (Janowiak et al. 2017).

2) MONTHLY CLIMATOLOGICAL PRECIPITATION

WorldClim 2 precipitation and PERSIANN–Climate Data Record (CDR) are utilized to generate global monthly climatological precipitation and serve as the secondary input for the deep learning model. WorldClim2 is a high-resolution precipitation dataset developed by Fick and Hijmans, derived from spatially interpolated weather station data (Fick and Hijmans 2017). It offers information on precipitation covering the period from 1970 to 2000 across global land areas. PERSIANN-CDR (Ashouri et al. 2015) is part of the PERSIANN family of precipitation datasets (Nguyen et al. 2019) and is an IR-based product that derives precipitation from geosynchronous satellite infrared observations, with calibration to gauge-based information. It provides precipitation data from 1983 to the present with a delay and accounts for precipitation over global water in the monthly climatological dataset. Implementing monthly climatological precipitation data has been tested and proven to enhance the accuracy of precipitation estimation (Nguyen et al. 2020a, 2020b).

3) IMERG V07 FINAL

Developed by NASA's Global Precipitation Measurement (GPM) mission, IMERG V07 integrates data from multiple satellite sources, including PMW and IR sensors, with ground-based gauge data to provide high-accuracy, gridded precipitation estimates at 0.1° spatial and half-hourly temporal resolution (Huffman et al. 2023a). It is important to note that IMERG V07 incorporates PDIR-Now as its infrared component, meaning that PUnet, which is trained on IMERG Final, has an indirect connection to PDIR-Now through this integration. IMERG V07 Final (hereafter referred to as IMERGF) serves as both the training target for deep learning models and the evaluation baseline for the PUnet precipitation estimates.

Validation studies indicate that IMERG Final performs well in regions with dense gauge networks, such as North America, Europe, and parts of Asia, effectively capturing moderate to heavy precipitation events. However, its accuracy diminishes over regions with sparse gauge coverage, including oceans, deserts, and mountainous terrains (Prakash et al. 2018; Nepal et al. 2021). Additionally, IMERG Final tends to overestimate light rainfall and underperform during snowfall events (Li et al. 2021). Continental-scale sub-daily evaluation indicates that IMERG V07 captures precipitation amounts with reasonable skill but shows regime and season dependent errors, including biases associated with overestimated precipitation frequency and underestimated intensity, and reduced skill for heavier hourly rates (Xiong et al. 2025). Over South America, comparative assessment of IMERG V07 versus V06 shows overall error reductions in V07 (e.g., lower RMSE in many regions), but also reports persistent difficulties in light-rain detection and underestimation in warm-cloud precipitation regimes (Rozante and Rozante 2024). IMERG performance has also been evaluated against ground-based gauge and radar products (e.g., Stage IV, MRMS, and GPCC) across a range of regions and precipitation intensities. The dataset is publicly available from NASA GES DISC (Huffman et al. 2023b).

b. Evaluation Data

1) PDIR-NOW

PDIR-Now is the latest product developed and released by UCI's CHRS, which provides near-real-time, high-resolution (0.04° × 0.04°) satellite precipitation estimates (Nguyen et al. 2020). As opposed to previous near-real-time precipitation datasets, PDIR-Now's primary benefit is that it uses frequently sampled IR imagery. PDIR-Now is ideally suited for near-real-time hydrologic applications like flood forecasting and creating flood inundation maps because of its low latency (15–60 min). The positive evaluation results suggest that the PDIR algorithm may be used to reconstruct historical precipitation estimates with high spatiotemporal resolution (Nguyen et al. 2020). PDIR-Now data (hereafter referred to as PDIR for simplicity), is available through the CHRS data portal (Nguyen et al. 2019), and provides hourly, 6-hourly, and daily temporal resolutions used in this study.

2) GLOBAL HYDRO ESTIMATOR (HE)

The current-generation operational algorithm has been used since 2002 (Scofield and Kuligowski 2003). HE precipitation estimates are produced every 15 minutes for the entire globe from 64°S to 64°N using available geostationary data over the Western Hemisphere (GOES); Europe, Africa, and western Asia (METEOSAT); and eastern Asia (Himawari). The system incorporates modern satellite imagery and atmospheric modeling techniques to produce near-real-time precipitation estimates, assisting meteorologists, hydrologists, and emergency responders in weather forecasting. In this study, HE at the hourly scale is accumulated into 6-hourly and daily scales, and all three temporal resolution are used as benchmark datasets for assessing PUnet's precipitation estimation performance.

3) STAGE IV

The National Centers for Environmental Prediction (NCEP) Stage IV (ST4) product is a national multi-sensor product composed of real-time gauge observations and WSR-88D radar data that covers the contiguous United States (CONUS). ST4 is a 4 km × 4 km gridded product available at hourly, 6-hourly, and daily resolutions. Precipitation estimates derived from a variety of sensors at the 12 regional National Weather Service (NWS) River Forecast Centers (RFCs) are manually quality-controlled before being mosaicked under NCEP supervision (Lin & Mitchell 2005). ST4 has been widely used in many previous SPP evaluations, such as the Tropical Rainfall Measuring Mission (TRMM), CMORPH, and PERSIANN, due to its long history of data production consistency (Beck et al. 2019; Sadegi et al. 2020; Mehran and AghaKouchak 2014). ST4 data is available at the Earth Observing Laboratory (EOL) data archive (Du 2011). The 1-hourly, 6-hourly (cumulative from hourly) and daily temporal resolution of NCEP ST4 data are utilized as ground-truth measurements in this paper to evaluate the performance of the PUnet estimation across the CONUS.

3. Methodology

a. Framework

The framework in Fig. 1 describes the process of integrating satellite imagery, climatological data, and image processing techniques to develop a global precipitation estimation model and produce the PUnet estimates. The main steps can be summarized as follows:

Data Processing: Inputs to the model consist of infrared (IR) images and monthly climatological precipitation data from the WorldClim 2 and PERSIANN-CDR datasets, while IMERG Final V07 precipitation estimates captured every 30 minutes between 2016 and 2021 serve as the target output during training. The dataset is processed by aggregating all half-hourly images for each calendar month across the 6-year record (total up to 8928 samples for a 31-day month); after preprocessing and quality control, we select 5,000 high-quality samples per calendar month for training, prioritizing instances with minimal missing-value pixels.

Prepared Data: All datasets are regridded to a common 512×1536 grid (~0.234°) before training. The model predictors include geostationary IR imagery (0.04°; 3000×9000 pixels) and static monthly climatological fields (WorldClim2 and PERSIANN-CDR). The training target is IMERGF precipitation (0.1°; 1200×3600 pixels). Both the inputs and the target are resampled using bilinear interpolation, balancing computational efficiency with spatial detail preservation. The 512×1536 input size was chosen to optimize the UNet's convolutional operations for global precipitation data, accommodating system and GPU memory limits while ensuring adequate spatial coverage and efficient training. An 80/20 split is used for training and validation purposes.

Monthly Model Training for 12 Months: For model training, a global UNet architecture is employed, with separate training conducted for each of the 12 months. This approach enables the model to capture seasonal variations in precipitation patterns, ensuring more accurate and reliable estimations throughout the year (Sha et al. 2020; Yang et al. 2023). Each monthly UNet model consists of a total of 7,782,337 parameters and undergoes 100 training epochs to optimize performance. After training the 12 models, both IR images and monthly climatological precipitation data for the desired period are used as input to generate new precipitation estimates. The input data must be preprocessed in the same manner as the training data to ensure consistency and accuracy in the predictions.

Bias Correction: The generated precipitation estimates are subjected to a single bias correction step to enhance accuracy. This method, Empirical Quantile Mapping (EQM), aligns the probability distribution of the UNet estimates with the reference IMERGF dataset.

Guided Filtering: To convert the output of the deep learning model (initial size 512x1536 or ~0.234°) back to the operational resolution of 0.04° (size 3000x9000), the bias-corrected

estimates are first downscaled to 3000x9000 using bilinear interpolation. Following downscaling, a guided filter is applied to reduce noise and preserve the cloud-shape information provided by the IR data. This step helps enhance the visual quality of the precipitation estimates, particularly following the interpolation process.

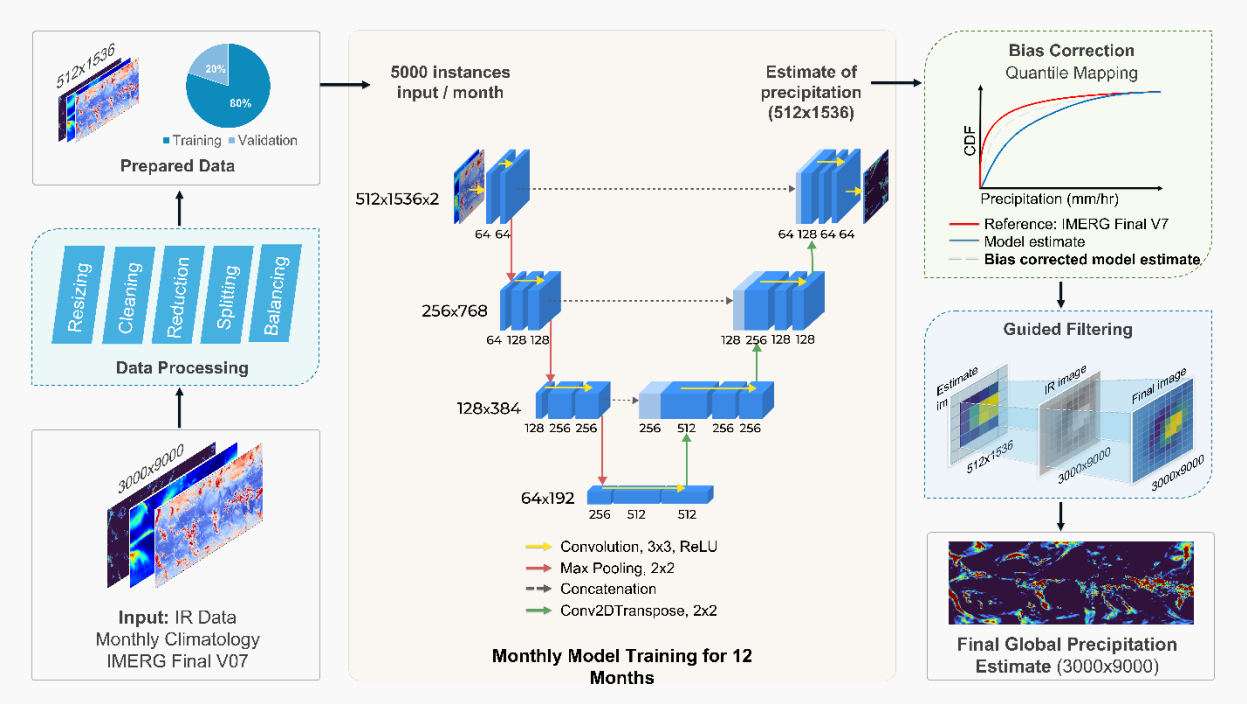


Fig. 1. Flowchart of the proposed PUnet workflow, showing its main process stages.

Detailed descriptions of the UNet model, bias correction methods, and guided filtering techniques are provided in the sub-sections below.

b. UNet Model

The UNet architecture features a distinctive U-shaped structure designed as an encoder-decoder framework, enabling the extraction of high-level features while preserving spatial details (Ronneberger et al. 2015). The encoder is the part of the network that compresses the input image into a smaller, more abstract representation. It works by applying layers of convolutions and pooling to gradually reduce spatial resolution while capturing important features (i.e., akin to conventional CNNs to capture context and abstract representations effectively). Conversely, the decoder reconstructs a detailed output from that compressed representation. It upsamples the features back to the original resolution (or to the desired output size) (Ji et al. 2018). In the UNet model used for PUnet estimations, the model inputs consist of

two 512x1536 matrices containing IR and monthly climatological precipitation data. These inputs undergo convolutions to encode spatial information and extract hierarchical features essential for accurate estimation. Three max-pooling operations are applied during convolution to downsample feature maps while retaining vital information, facilitating the capture of local and global context. Following encoding, convolutional layers are upsampled to match the original input size. Concatenation merges feature maps from the encoding and decoding paths to restore spatial details lost during downsampling. Subsequently, 2D convolutional layers in the decoder refine the upsampled feature maps. Finally, the output layer comprises a single convolutional layer with a rectified linear unit (ReLU) activation function, presenting the predicted image corresponding to the inputs. Mean Squared Error (MSE) serves as the loss function for the Unet model, and training is performed using the Adam gradient descent optimizer with a learning rate set at 0.0001. The training process was conducted for up to 100 epochs with a batch size of 8, employing early stopping with a patience of 15 epochs based on validation loss to prevent overfitting and ensure optimal generalization. The proposed UNet architecture with details of input shapes, convolutional layers, and operations for global precipitation estimations is also shown in Fig. 1.

Additionally, Fig. 2 shows the learning curves for six selected monthly models (January, March, May, July, September, and November), with the blue line representing the training loss and the orange line representing the validation loss. Training loss is calculated on the data used to fit the model, while validation loss is calculated on a separate held-out dataset and is used to assess how well the model generalizes and whether overfitting is occurring. In all models, the training loss decreases rapidly and smoothly during the first 40 epochs and becomes relatively stable after epoch 60. Similarly, the validation loss decreases greatly, with minor fluctuations during the first 40 epochs, and then stabilizes and aligns closely with the training loss after epoch 60. Both the training and validation losses steadily converged, indicating good generalization capability of the PUnet model. It is noteworthy that the learning curves for the months not shown exhibit similar behavior without overfitting issues, highlighting the consistency of the data processing and training approaches.

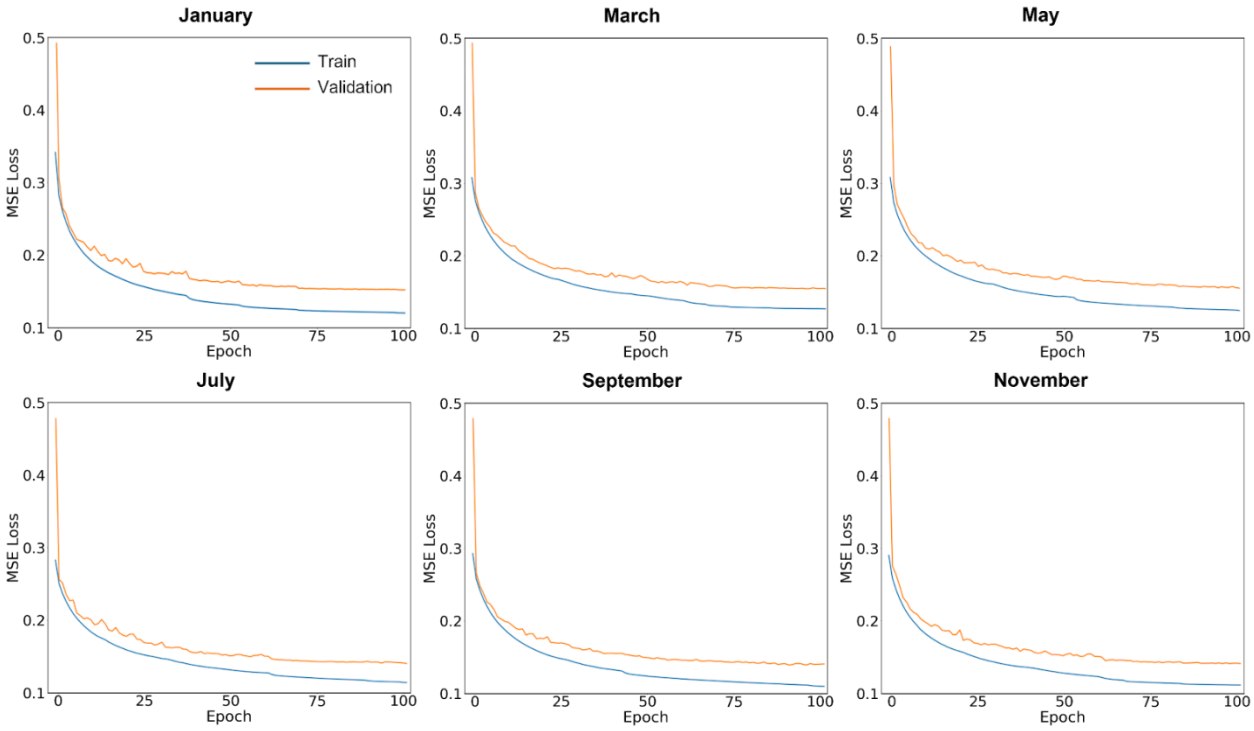


Fig. 2. PUnet learning curves (100 epochs) for six representative months: January, March, May, July, September, and November.

c. Bias Correction Technique

After generating new estimates, bias correction techniques are employed to enhance the accuracy and reliability of predictions.

Due to its simplicity and effectiveness, quantile mapping is a widely adopted technique for bias correction in precipitation data (Maraun et al. 2010; Enayati et al. 2021). This technique aligns the corresponding quantiles of the modeled and observed datasets, ensuring that both the frequency and intensity of precipitation events are corrected to more accurately reflect local conditions. However, it has limitations, such as its reliance on the assumption that the distribution of biases remains constant across time, and its inability to capture complex, non-linear relationships that may exist in the data (Cannon et al. 2015).

This study applies empirical quantile mapping (EQM) to align the probability distribution of PUnet estimates with the reference IMERGF data by matching the k'th quantile of the model distribution to the corresponding k'th quantile of the observed data distribution. Data from the training period were used to calculate 20 pre-defined quantiles for both the model and historical

distributions. Once the model produces estimates, the mapping process is applied to each pixel to adjust its value according to the calculated quantiles, ensuring consistency with the reference data (Cannon et al. 2015). Mathematically, the EQM correction can be summarized as:

$$P_{corrected} = F_{obs}^{-1}(F_{model}(P_{model})) \quad (1)$$

Where $P_{corrected}$ refers to bias-corrected precipitation estimate, P_{model} represents the modeled precipitation value at each grid point, F_{model} denotes the empirical cumulative distribution function of the modeled data, and F_{obs}^{-1} is the inverse of the empirical cumulative distribution function of the observed data, also referred to as the quantile function (Cannon et al. 2015).

d. Guided Filtering

To further enhance the quality and resolution of the precipitation estimates, guided filtering is employed. This includes downscaling the newly estimated precipitation data back to IR's original resolution of 3000x9000 pixels and performing guided filtering based on high-resolution IR data. Known for its high efficiency and exceptional edge-preserving capability, guided image filtering is a widely used local filtering technique (He et al. 2012; Lu et al. 2018). This step helps reduce noise and enhance spatial coherence, resulting in precipitation maps with improved apparent resolution and visual clarity.

In our model, guided filtering operates on two images: the input image *I* (3000x9000 image after downscaling) and a guidance image *g* (3000x9000 IR data). The goal is to compute an output image *P* that is a smoothed version of *I* while maintaining the structural details provided by *g*.

For each pixel (*i,j*), the output *P* is given by:

$$P(i,j) = a(i,j) \cdot I(i,j) + b(i,j) \quad (2)$$

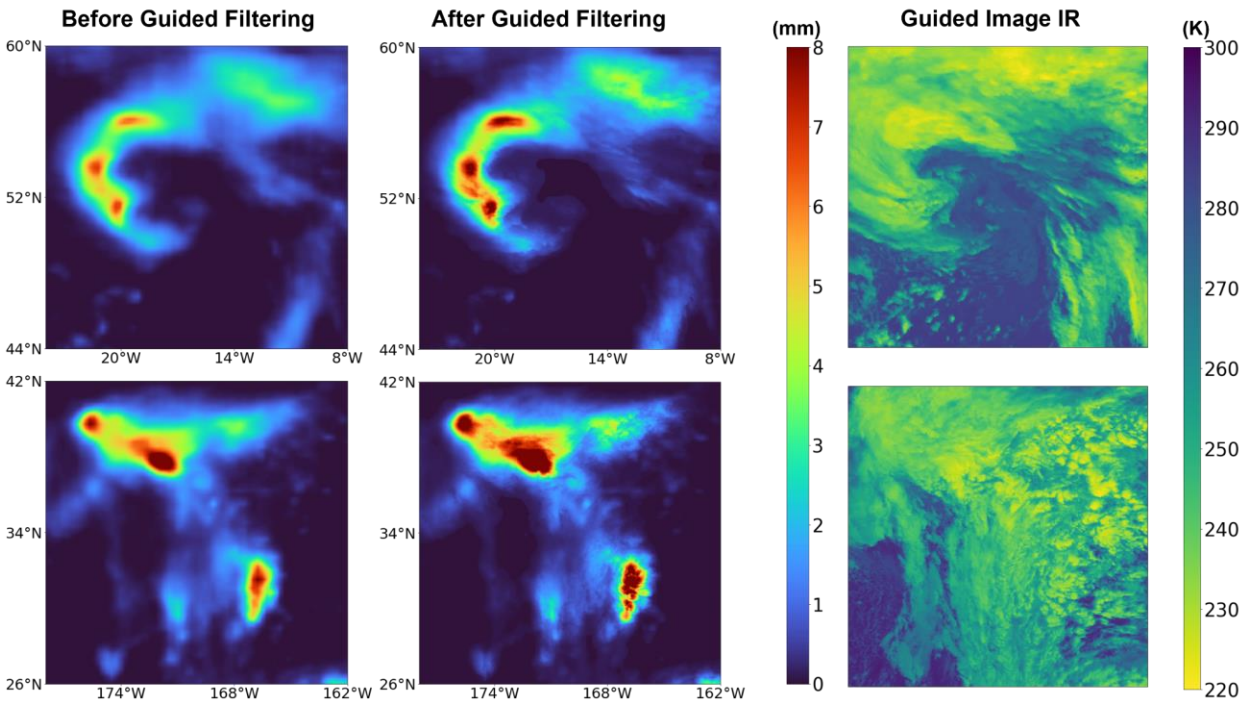
Where *a(i,j)* and *b(i,j)* represent spatially varying linear parameters defined within a local neighborhood window. The parameters *a(i,j)* and *b(i,j)* are computed based on the guidance image g and the input image I within a predefined local window:

$$a(i,j) = \frac{Cov(I,g) + \epsilon}{Var(g) + \epsilon} \quad (3)$$

$$b(i,j) = \mu_I - a(i,j) \cdot \mu_g \quad (4)$$

Where *Cov(I,g)* is the covariance between *I* and *g*, *Var(g)* is the variance of g, μ_I and μ_g are the mean values of *I* and *g* within the local window. ϵ is a regularization parameter to prevent division by zero and control the smoothness (He et al. 2012). The local window of 15x15 pixels and ϵ of 0.0001 are set in the current PUnet operation.

Fig. 3 presents two zoomed-in views that highlight the role of the guided filtering process in enhancing the apparent resolution and visual clarity of half-hourly precipitation estimates after the downscaling of the model output. The first column shows the precipitation estimates at 0.04° resolution (3000 × 9000 grid) obtained through bilinear interpolation from the model output size of 512 × 1536. As is common with interpolation, the results exhibit blurring and a loss of spatial detail. The guided filtering technique introduced above is applied to address this issue, leveraging high-resolution IR data while preserving the precipitation patterns produced by the model and maintaining water balance. The improved estimates, shown in the second column, clearly demonstrate enhanced spatial detail while faithfully retaining the original precipitation structures. Although local precipitation appears increased in the zoomed-in windows, the global mean precipitation is conserved (0.1209015 mm before vs. 0.1209016 mm after filtering), and this conservation holds for all cases. For reference, the high-resolution IR input used for guidance is displayed in the third column, illustrating the strong influence of the high-frequency information incorporated through the guided filtering process.



372

373 **Fig. 3**. Zoomed-in view of precipitation estimates from the PUnet model before and after
374 applying guided filtering, using the IR image as guidance.

375 *e. Performance Metrics*

376 The statistical metrics used in this study include the Correlation Coefficient (CORR), Root
377 Mean Squared Error (RMSE, in mm), Mean Absolute Error (MAE, in mm), relative bias (rBIAS,
378 in %), Probability of Detection (POD), False Alarm Ratio (FAR), and Critical Success Index
379 (CSI); the corresponding formulas are provided below. Here, P_i denotes the evaluated
380 precipitation estimate (e.g., PUnet) and R_i denotes the reference precipitation (e.g., IMERGF,
381 ST4); $\underline{P}$ and $\underline{R}$ are their respective means, and n is the number of matched samples (pixels and
382 times) used in the evaluation.

383 $$CORR = \frac{\sum_{i=1}^{n}(P_i - \underline{P})(R_i - \underline{R})}{\sqrt{\sum_{i=1}^{n}(P_i - \underline{P})^2}\sqrt{\sum_{i=1}^{n}(R_i - \underline{R})^2}} \quad (5)$$

384 $$RMSE\ (mm) = \sqrt{\frac{1}{n}\sum_{i=1}^{n}(P_i - R_i)^2} \quad (6)$$

385 $$MAE\ (mm) = \frac{1}{n}\sum_{i=1}^{n}|P_i - R_i| \quad (7)$$

$$rBIAS\ (\%) = \frac{\sum_{i=1}^{n}(P_i - R_i)}{\sum_{i=1}^{n} R_i} \times 100 \quad (8)$$

$$POD = \frac{TP}{TP+FN} \quad (9)$$

$$FAR = \frac{FP}{TP+FP} \quad (10)$$

$$CSI = \frac{TP}{TP+FP+FN} \quad (11)$$

4. Results and Discussion

a. Global Evaluation

The evaluation of global precipitation estimation is crucial for understanding and improving weather prediction, climate monitoring, and water resource management. This section compares the performance of HE, PDIR, and PUnet (the model developed in this paper), to IMERG V07 Final, which is the target of the PUnet algorithm and ingests PDIR in its retrieval scheme. The comparison is conducted over the 2022-2023 period, which was not used in PUnet training.

1) ANNUAL ANALYSIS

Fig. 4 illustrates the mean global annual precipitation from IMERGF (reference, right panel) and differences relative to IMERGF for HE, PDIR, and PUnet during 2022–2023, and provides a summary of key comparison metrics, including CORR, RMSE, rBIAS, and MAE, with IMERGF serving as the reference. In this study, rBIAS represents the percentage difference between PUnet and the reference, where positive values indicate overestimation and negative values indicate underestimation. MAE represents the average magnitude of the error regardless of sign, providing a measure of overall accuracy. When compared to other operational products, PUnet demonstrates outstanding performance, achieving the highest CORR of 0.98, indicating strong agreement with the reference dataset IMERGF. This high correlation suggests that PUnet is skilled in capturing global precipitation patterns. PUnet also exhibited the lowest RMSE of 201.90 mm, much lower than that of HE (366.78 mm) and PDIR (298.28 mm), indicating its capability in minimizing errors in precipitation estimation. Its relative BIAS of +1.3% corresponds to only a slight positive deviation compared to the reference, while the MAE of

133.65 mm is the smallest among the three products, further demonstrating its ability to capture IMERGF precipitation. Additionally, PUnet shows smaller deviations from IMERGF than HE and PDIR, as illustrated in Fig. 4. Although PUnet does not display the unrealistic artifacts present in HE, it exhibits a similar precipitation discontinuity near ~90°E as seen in PDIR.

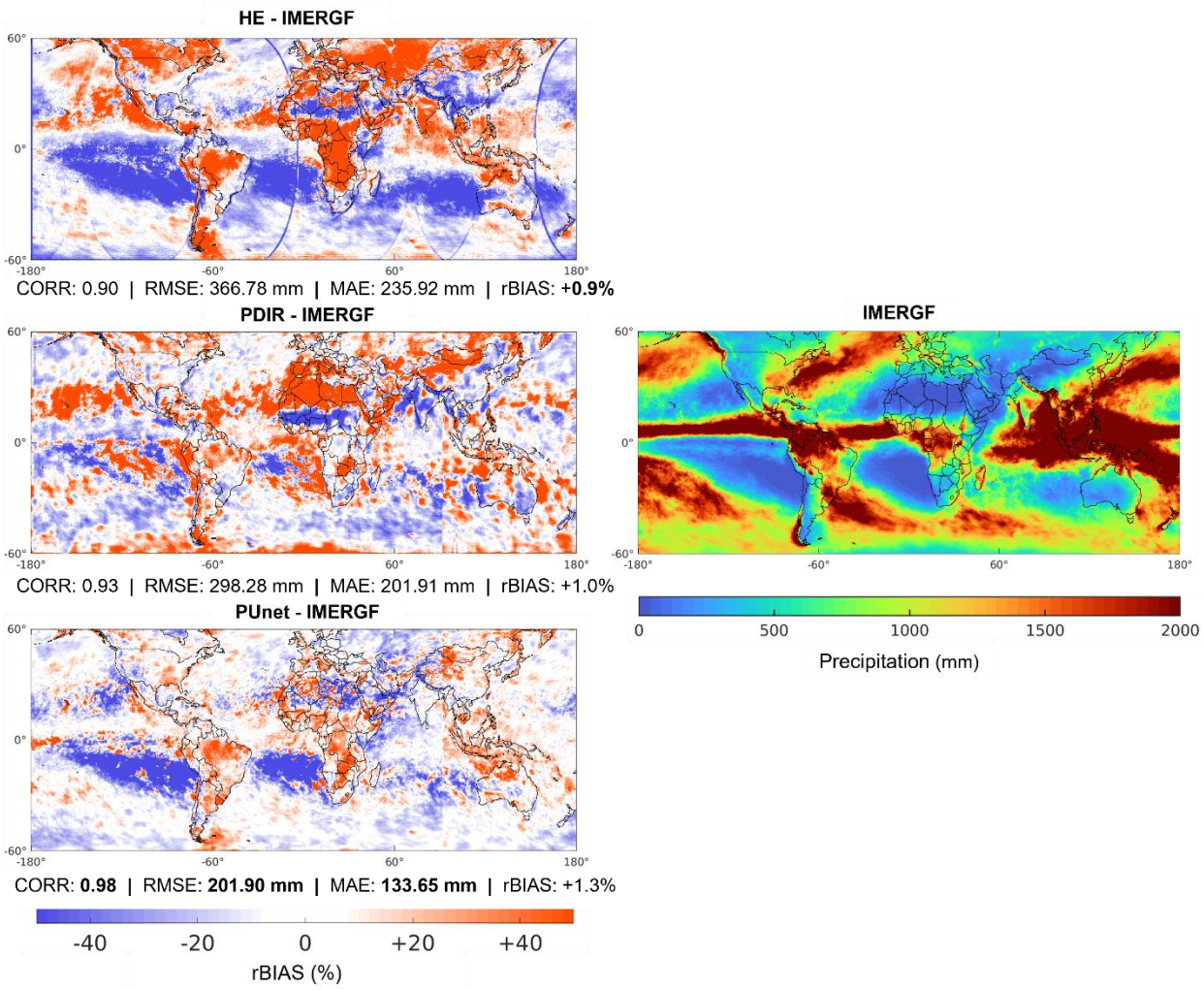


Fig. 4. Mean global annual precipitation (mm) from IMERGF (reference, right panel) and differences relative to IMERGF for HE, PDIR, and PUnet during 2022–2023. Evaluation metrics are shown for each dataset (bold values indicating the best performance).

The analysis of the meridional mean annual precipitation for the period 2022–2023 across four datasets—HE, PDIR, PUnet, and IMERGF—reveals variations in the models' ability to capture precipitation patterns across different longitudes (Fig. 5). PUnet and PDIR align most closely with the reference IMERGF across all longitudes, which is expected given their

dependency on IMERG (PDIR is incorporated into IMERG, and IMERG is used as the training target for PUnet). Minor discrepancies are observed, such as slight positive deviations relative to IMERGF near 60°W over the Amazon Basin and negative deviation around 70°E, particularly over the western Indian Ocean. These biases may be attributed to the limited sensitivity of IR-based inputs to warm rain processes prevalent in this region, which can lead to underdetection of precipitation (Ombadi et al. 2021). For the zonal analysis (Fig. 5), PUnet consistently demonstrates the best alignment with IMERGF, across various latitudinal bands. This is expected due to PUnet being trained to target IMERGF, representing a key success of the model's design. The only noticeable variation in the precipitation estimates occurs near the equator. This discrepancy may be attributed to the complex atmospheric and oceanic processes that dominate this region. The equatorial zone is influenced by factors such as the Intertropical Convergence Zone (ITCZ), which causes significant variability in precipitation patterns (Dezfuli 2017; Nicholson 2018). Additionally, the presence of tropical cyclones and monsoonal systems further complicates accurate precipitation estimation (Chang et al. 2013; Green et al. 2020). As such, these challenges may result in small deviations in model performance, even when the overall alignment with IMERGF remains strong. Another feature in the meridional mean is a sharp jump in both PDIR and PUnet near 90°E, likely inherited from the upstream infrared input fields, which are mosaicked from multiple satellite views. Such mosaicking can introduce radiometric or resampling discontinuities at stitch boundaries that propagate into the retrievals and appear in global bias patterns (Figure 4), with the effect being less pronounced in PUnet than in PDIR.

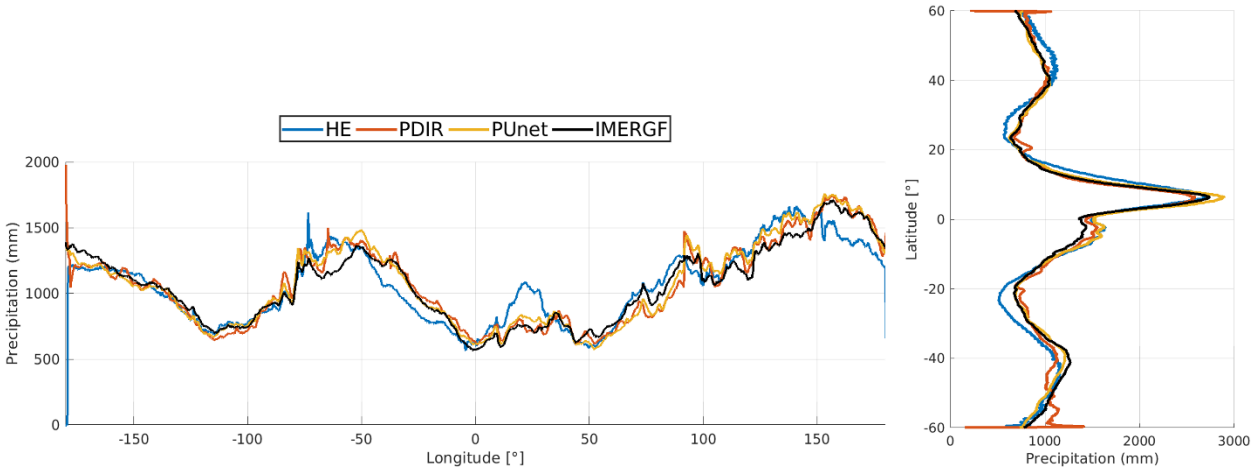


Fig. 5. (left) Meridional mean and (right) Zonal mean annual precipitation for the period (2022–2023) for HE (blue), PDIR (orange), PUnet (yellow), and IMERGF (black).

2) Monthly Analysis

Here, we examine the performance of PUnet in capturing the seasonal cycle of precipitation based on monthly precipitation at the global scale, against the spaceborne reference IMERGF. Fig. 6 illustrates the mean global monthly precipitation, CORR, RMSE, rBIAS, and MAE during the evaluation period (2022-2023) for the four different precipitation estimation datasets: HE (blue), PDIR (orange), PUnet (yellow), and IMERGF (black).

Overall, in terms of mean monthly precipitation, both PUnet and HE demonstrate the closest alignment with the reference dataset, IMERGF, implying their reliability in replicating observed precipitation patterns. PUnet performs consistently well throughout the year, although its precipitation estimates slightly exceed those of IMERGF during the spring months of March, April, and May. In contrast, PDIR tends to exceed monthly precipitation, particularly during the Northern Hemisphere winter season (December to February). This trend is further reflected in the rBIAS index, which reveals the relative accuracy of PUnet and HE, as their bias values remain closer to the zero-bias line, indicating minimal systematic errors in comparison to others.

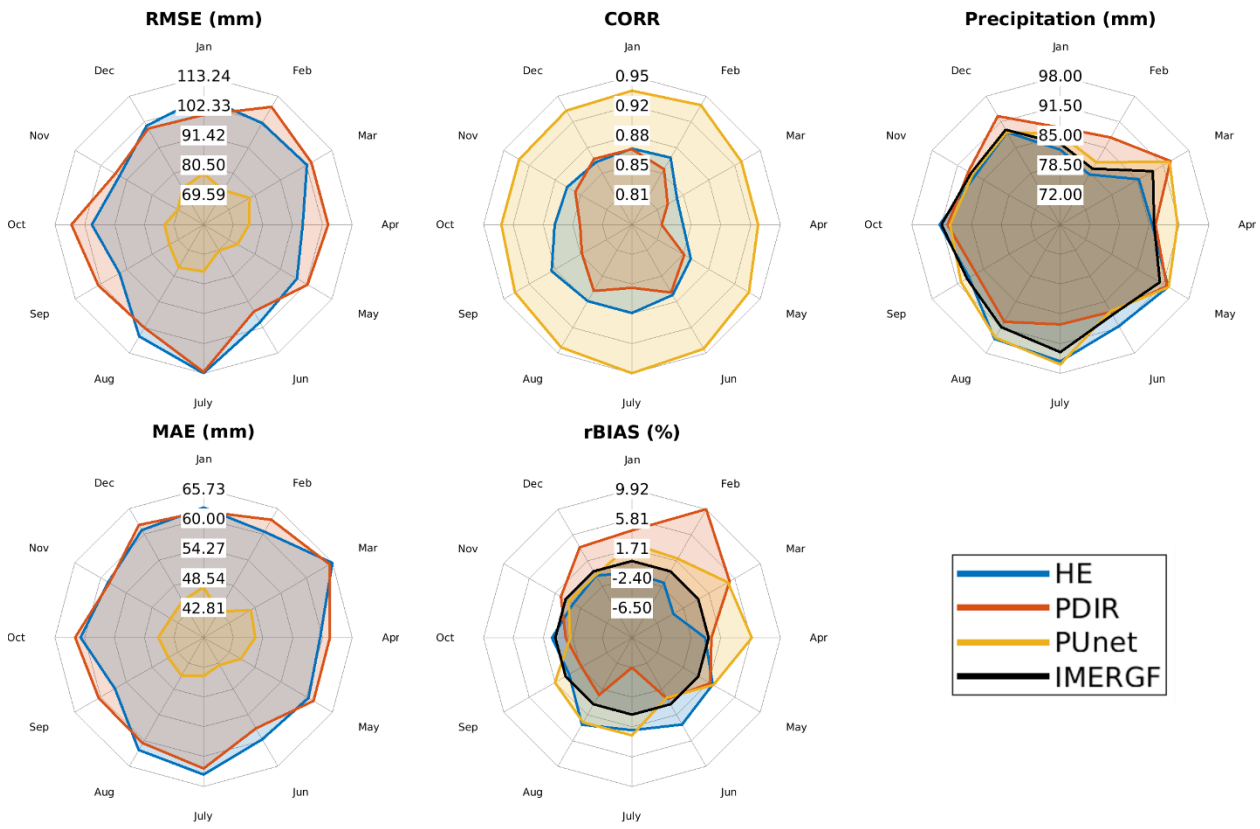


Fig. 6. Mean global monthly precipitation, CORR, RMSE, rBIAS, and MAE during the evaluation period (2022-2023) for HE (blue), PDIR (orange), PUnet (yellow), and IMERGF (black).

Regarding CORR, the PUnet model demonstrates the strongest performance, consistently maintaining values above 0.92 threshold, whereas HE and PDIR exhibit lower values ranging from 0.81 to 0.88. It should be noted, however, that this superior agreement is expected since PUnet is explicitly trained to target IMERG and thus inherently aligns more closely with the reference compared to other IR-based datasets. In terms of RMSE and MAE, PUnet shows lower error values than the other products, reflecting its design rather than a shortcoming of the other products. PUnet's performance metrics, particularly RMSE and MAE, remain stable throughout the year.

3) Hourly Analysis

The summary statistics presented in Table 2 provide a comparative assessment of global hourly precipitation estimates for 2022 from HE, PDIR, and PUnet, using IMERGF as the

spaceborne reference. Across the global domain, PUnet demonstrates the strongest agreement with IMERGF, achieving the highest correlation (CORR = 0.67), along with the lowest RMSE (0.54 mm) and MAE (0.11 mm), indicating improved representation of both precipitation variability and magnitude at the hourly scale. The relative bias of PUnet (−3%) indicates a small systematic negative bias, comparable to HE (−2%) and smaller in magnitude than the positive bias exhibited by PDIR (+4%).

These results should be interpreted in the context of the methodological interdependencies with IMERG. PUnet is explicitly trained on IMERG precipitation, which inherently promotes statistical consistency with the reference dataset, whereas PDIR represents the infrared-based input to IMERG and therefore reflects the limitations of IR-only retrievals at sub-daily timescales. This distinction is evident in the lower CORR (0.50) and higher RMSE (0.67 mm) of PDIR relative to PUnet.

Categorical metrics in Table 2 further highlight the improved detection skill of PUnet, which achieves the highest POD (0.56) and lowest FAR (0.40), resulting in the largest CSI (0.41) among the evaluated products. In contrast, both HE and PDIR exhibit lower CSI values (0.29 and 0.27, respectively). Overall, the hourly evaluation demonstrates that PUnet provides the most consistent performance relative to IMERGF, while also illustrating the added value of learned IR–precipitation mappings beyond raw IR-based retrievals.

Table 2. Summary statistics of comparison metrics for global hourly precipitation in 2022: CORR, RMSE, BIAS, POD, FAR, and CSI for HE, PDIR, and PUnet with IMERGF as spaceborne reference (bold values indicate the best performance).

	HE	**PDIR**	**PUnet**
Continuous			
CORR	0.46	0.50	**0.67**
RMSE (mm)	0.56	0.67	**0.54**
rBIAS (%)	**-2**	+4	-3
MAE (mm)	0.13	0.14	**0.11**
Categorical			
POD	0.45	0.41	**0.56**
FAR	0.55	0.56	**0.40**
CSI	0.29	0.27	**0.41**

b. CONUS Evaluation

1) Annual Analysis

In transition from the global scale, we next evaluate the precipitation estimates over the contiguous United States (CONUS) region to examine model performance against a high-quality reference. The evaluation covers the period from 2022 to 2023 and again includes four different precipitation estimation datasets: HE, PDIR, PUnet, and IMERGF, now with ST4 serving as the ground-based reference. Unlike spaceborne references, ST4 integrates observations from a dense network of ground-based radars and rain gauges, thus providing more trustworthy and representative measurements of near-surface precipitation. This regional assessment is therefore critical, as it provides insights into the effectiveness and reliability of satellite-based products in a region characterized by diverse climatic conditions and varying precipitation patterns.

Fig. 7 illustrates the mean annual precipitation estimates from ST4 (reference, right panel) and differences relative to ST4 for HE, PDIR, PUnet, and IMERGF during 2022–2023. The analysis reveals that all models tend to overestimate precipitation in the southeastern CONUS, as evidenced by the high positive biases. IMERGF and PUnet stand out with the highest CORR of 0.90, indicating a strong agreement with the spatial pattern of annual ST4. Although PUnet's RMSE of 294.61 mm is higher than IMERGF's 247.18 mm, it remains competitive relative to the other two IR datasets. PUnet's rBIAS of +32% suggests a moderate level of overestimation, while its MAE of 215.26 mm is favorable compared to HE (277.70 mm) and aligns closely with IMERGF and PDIR.

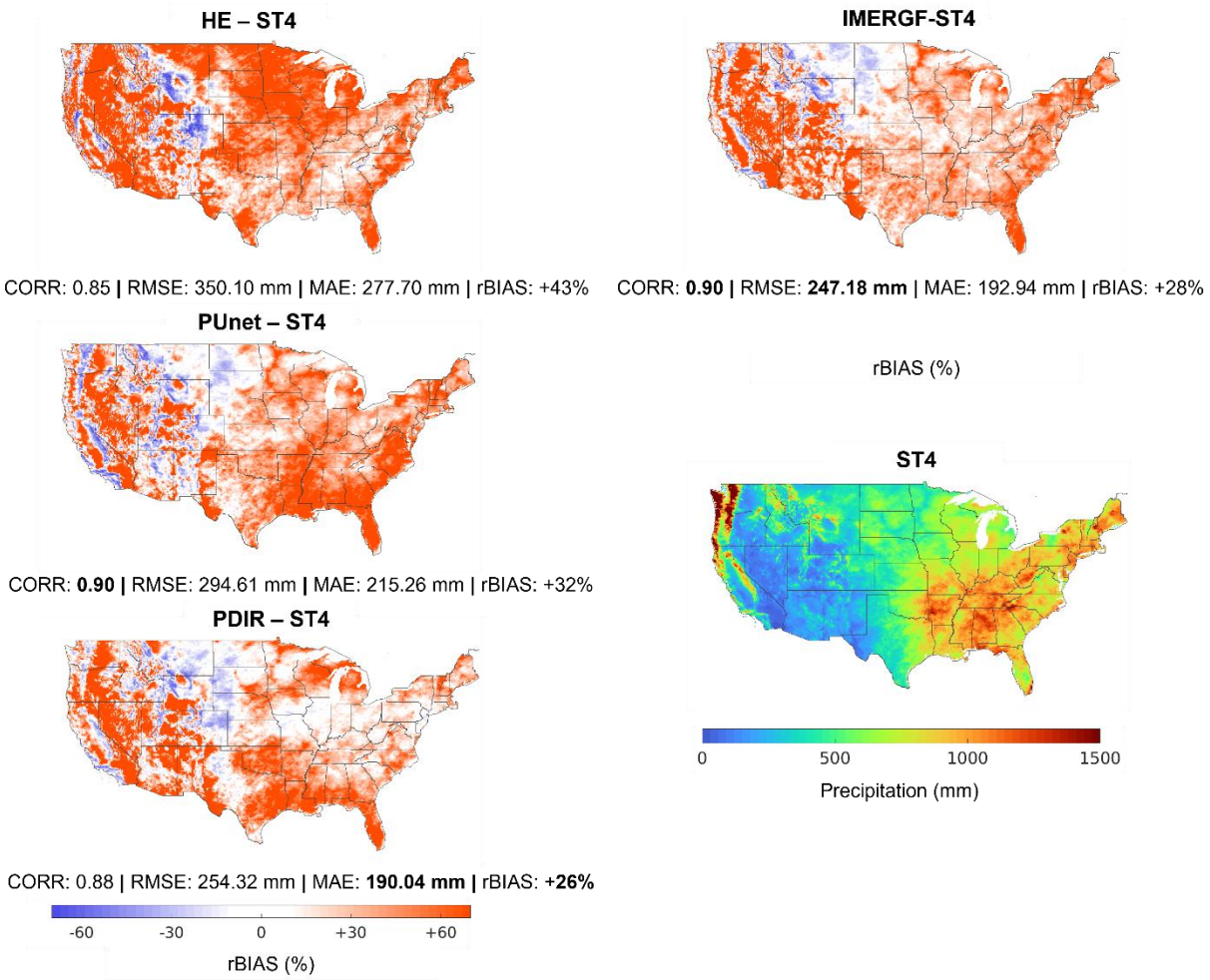


Fig. 7. Mean global annual precipitation (mm) from ST4 (reference, right panel) and differences relative to ST4 for HE, PDIR, PUnet, and IMERGF during 2022–2023. Evaluation metrics are shown for each dataset (bold values indicate the best performance).

Although PUnet demonstrates overestimation in the southeastern United States, its long-term annual mean estimates along the west coast, including Washington, Oregon, and California, are more consistent with the reference on average. However, the model's output for the central part of the CONUS exhibits a smoother pattern compared to ST4 and IMERGF products. The observed smoothness arises primarily from the coarse model output resolution (~0.234°), due to computational limitations, as higher-resolution modeling would require substantially more computing resources. This limitation in spatial detail is compounded by the local averaging introduced during the convolutional operations of the UNet architecture (Ayzel et al. 2019; Ravuri et al. 2021). While guided filtering can enhance spatial features at the sub-daily scale, the effect becomes less pronounced in monthly and yearly accumulations due to the nature of the

model outputs, particularly in regions characterized by complex and highly variable precipitation patterns.

2) Hourly Analysis

As shown in Table 3, IMERGF exhibits the strongest agreement with the reference dataset ST4 over the CONUS region for hourly precipitation in 2022, achieving the highest correlation (CORR = 0.58). PUnet follows with a CORR of 0.48, demonstrating clear improvement over both HE (0.28) and PDIR (0.37). Part of the observed performance contrast may be attributed to the data foundations of the products, with PDIR relying only on infrared measurements and PUnet relying on IMERG-derived training that incorporates radar, passive microwave, and gauge information.

In terms of error metrics, IMERGF maintains the lowest RMSE (0.51 mm) and MAE (0.08 mm), reflecting its superior accuracy relative to ST4. Among the IR-based products, PUnet exhibits the lowest RMSE (0.65 mm) and MAE (0.10 mm), outperforming both HE and PDIR. All products show a positive relative bias, indicating a general tendency to overestimate hourly precipitation over CONUS, with IMERGF exhibiting the smallest bias (+2%) and larger biases observed for HE (+11%), PUnet (+10%), and PDIR (+7%).

Table 3. Summary statistics of comparison metrics for CONUS hourly precipitation in 2022: CORR, RMSE, BIAS, MAE, POD, FAR, and CSI for HE, PDIR, PUnet, and IMERGF with ST4 as reference (bold values indicate the best performance).

	HE	**PDIR**	**PUnet**	**IMERGF**
Continuous				
CORR	0.28	0.37	0.48	**0.58**
RMSE (mm)	0.68	0.71	0.65	**0.51**
rBIAS (%)	+11	+7	+10	**+2**
MAE (mm)	0.12	0.12	0.10	**0.08**
Categorical				
POD	0.40	0.28	0.44	**0.55**
FAR	0.69	0.70	0.55	**0.44**
CSI	0.21	0.17	0.29	**0.38**

For categorical metrics, IMERGF again demonstrates the strongest detection capability with the highest POD (0.55) and lowest FAR (0.44), resulting in the largest CSI (0.38). Among the remaining products, PUnet achieves the highest POD (0.44) and the lowest FAR (0.55), yielding

a CSI of 0.29 and indicating improved event detection and reduced false alarms relative to HE and PDIR. In contrast, PDIR exhibits the lowest POD (0.28) and highest FAR (0.70), leading to the smallest CSI (0.17), consistent with the limitations of IR-only retrievals for hourly precipitation over CONUS. Overall, while IMERGF provides the strongest performance against ST4, PUnet remains competitive among the evaluated products and demonstrates added value relative to raw IR-based estimates at the hourly scale.

3) Extreme Indices Analysis

To further evaluate PUnet, we now focus on extreme precipitation indices over CONUS. Specifically, we consider the following: (i) the number of days with daily precipitation ≥ 10 mm (R10mm), the maximum number of consecutive wet days (CWD), and the maximum number of consecutive dry days (CDD); (ii) the total precipitation from days exceeding the 95th and 99th percentiles (R95pTOT and R99pTOT, respectively); and (iii) the Simple Daily Intensity Index (SDII), defined as total precipitation divided by the number of wet days over the period of interest. Formal definitions follow Nguyen et al. (2018), and all acronyms and definitions are summarized in Table 4.

Fig. 8 presents six extreme precipitation indices for several datasets (PDIR, HE, PUnet, IMERGF) compared to the reference ST4 over the CONUS. According to Table 4, the models exhibit varying degrees of alignment with the reference ST4. For example, SDII values range from 7.54 mm/day (PDIR) to 9.12 mm/day (PUnet), with PUnet slightly overestimating compared to ST4's 8.50 mm/day. The CDD index shows significant differences, with PUnet predicting the close value of dry spells (43.77 days) to ST4's 48.14 days, while PDIR estimates the shortest duration of 15.97 days. Similarly, the CWD index varies with PDIR showing the longest consecutive wet periods (18 days), which surpasses the ST4 reference value of 5.10 days, while PUnet (6.59 days) and IMERGF (6.88 days) provide closer approximations to ST4. In terms of R10mm, PDIR (36.69 days), PUnet (43.87 days), and IMERGF (43.39 days) align more closely with the reference (35.01 days) than HE (51.94 days). Regarding extreme precipitation totals, PUnet overestimates precipitation during very wet and extremely wet days compared to ST4 with high R95pTOT and R99pTOT (879.08 mm and 322.11 mm, respectively). This overestimation suggests that while PUnet performs well in detecting moderate precipitation events, it may be less accurate in capturing extreme precipitation events.

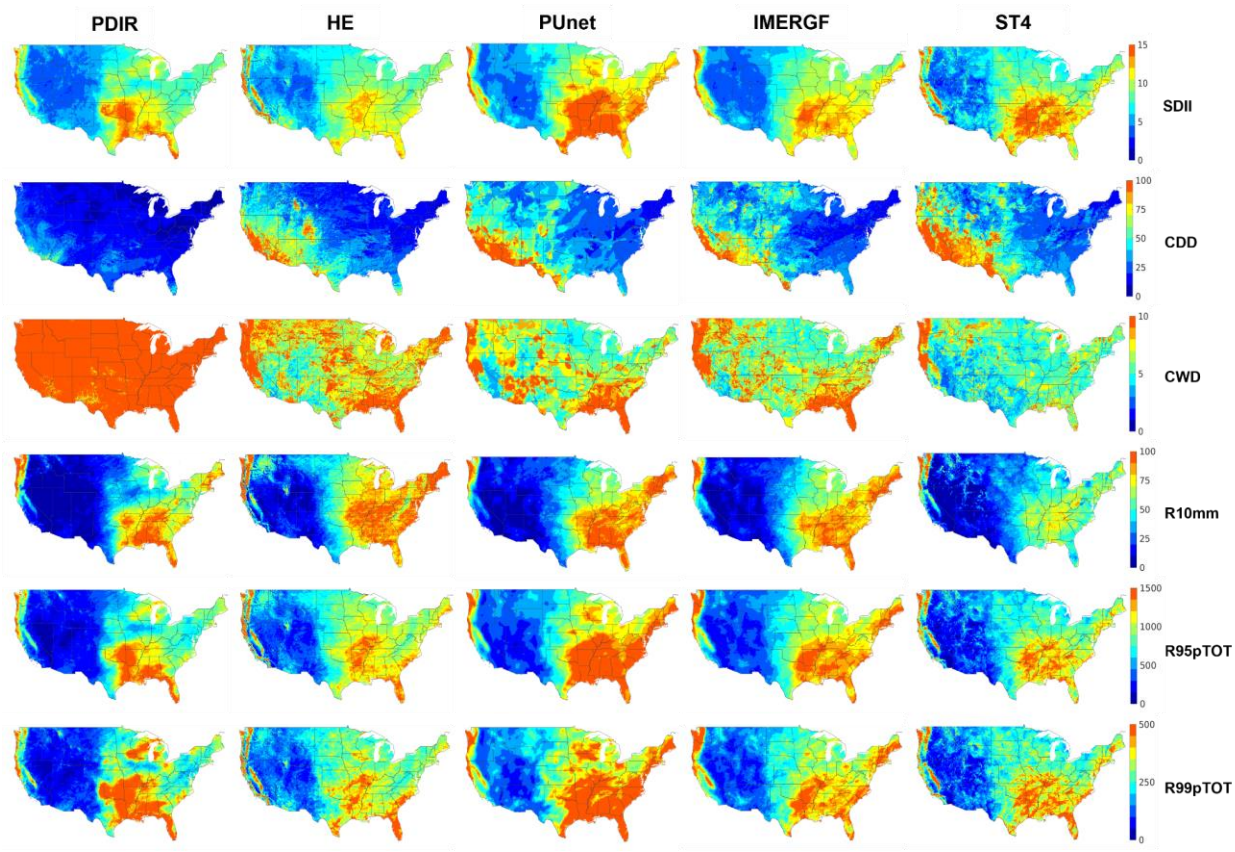


Fig. 8. Extreme precipitation indices (SDII, CDD, CWD, R10mm, R99pTOT, and R95pTOT) for PDIR, HE, PUnet, IMERGF, and ST4 over the CONUS.

In comparison to the other IR products, PUnet demonstrates competitive performance in capturing extreme precipitation patterns; however, its extreme indices do not consistently align more closely with IMERGF than those of HE (i.e., SDII, CDD, R95pTOT, and R99pTOT). PUnet exhibits a higher SDII, indicating a tendency to predict more intense daily precipitation, but it shows a level of agreement with the reference ST4 in terms of R10mm, CDD, and CWD, suggesting a reasonable representation of consecutive dry and wet spells. However, PUnet tends to overestimate both R95pTOT and R99pTOT, revealing a propensity to exaggerate total precipitation from very wet and extremely wet days. Although PUnet effectively captures certain patterns of extreme precipitation indices, there is still potential for improvement in balancing its intensity and frequency estimates.

Table 4. Extreme indices definition and summary statistics for HE, PDIR, PUnet, IMERGF, and ST4 over the CONUS.

Index	***Definition***	***Unit***
SDII	Simple daily intensity index	mm day^{-1}

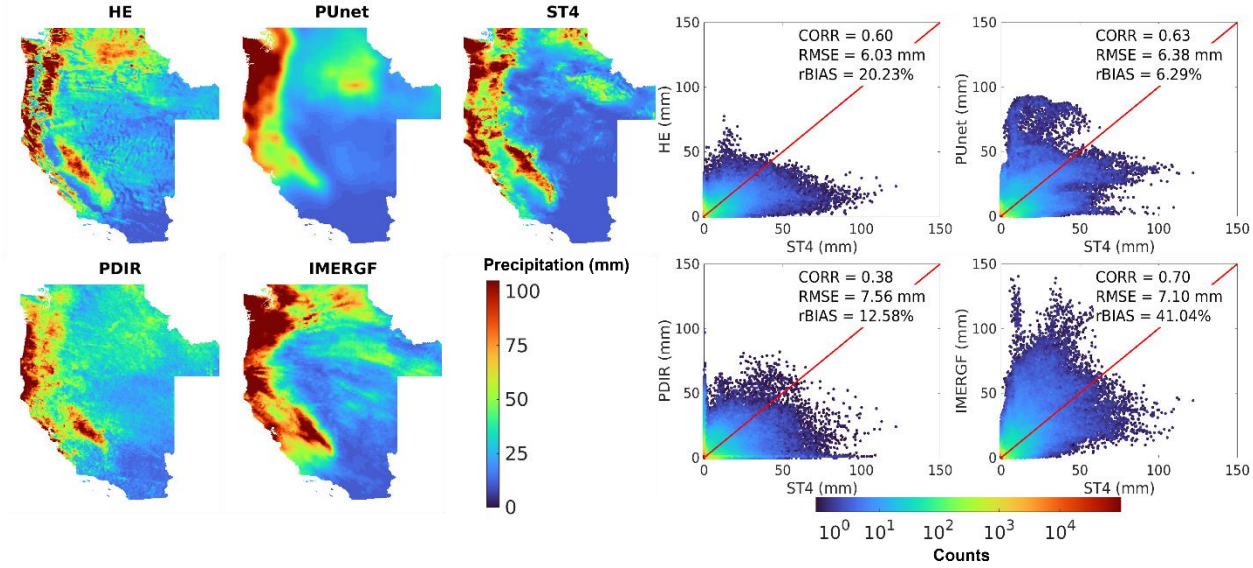
CDD	Annual maximum number of consecutive days with daily precipitation < 1mm	days
CWD	Annual maximum number of consecutive days with daily precipitation ≥ 1mm	days
R10mm	Annual count of days when daily precipitation amount > 10 mm	days
R95pTOT	Annual total precipitation when daily precipitation amount > 95th percentile	mm
R99pTOT	Annual total precipitation when daily precipitation amount > 99th percentile	mm

606

	HE	PDIR	PUnet	IMERGF	ST4
Extreme indices					
SDII (mm/day)	8.00	7.54	9.12	**8.04**	8.50
CDD (days)	36.93	15.97	**43.77**	39.80	48.14
CWD (days)	7.60	18.00	**6.59**	6.88	5.10
R10mm (days)	51.94	**36.69**	43.87	43.86	35.01
R95pTOT (mm)	796.18	**637.68**	879.08	791.99	711.73
R99pTOT (mm)	**265.74**	247.38	322.11	272.56	260.04

607 *c. Case study: Western US Evaluation*

608 Fig. 9 presents the precipitation accumulation from the PUnet model during the extreme
609 event of December 26–27, 2022, compared to other products, with ST4 as the reference.
610 IMERGF exhibits patterns similar to ST4 but tends to overestimate precipitation in regions such
611 as Southern California, Washington, and Montana. In contrast, while HE and PDIR provide
612 more accurate estimates along the coast, they overestimate precipitation in inland areas.
613 Although PUnet has a lower resolution and smoother characteristics, it effectively captures the
614 overall precipitation pattern and notably avoids the overestimation issues observed in the other
615 products.



616

Fig. 9. Accumulated precipitation maps and scatter plots over the Western US for the period 26-27 December 2022 for HE, PDIR, PUnet, IMERGF, compared to ground truth ST4.

To further evaluate the performance of PUnet over the Western U.S. during this extreme event, scatter plots of 6-hour precipitation from December 26–27, 2022, are presented in Fig. 9 (right side), comparing HE, PDIR, PUnet, and IMERGF (arranged from top to bottom and left to right) to the ground reference ST4. The colorbar represents the number of points (on log10 scale) at each location in the scatter plot, with warmer colors indicating higher data density. This visualization, together with the accompanying statistical metrics, provides a clear comparison of how each model's estimates correspond to observed values under same event conditions. As indicated by the summary statistics in the scatter plots, the CORR values range from 0.38 for PDIR to 0.70 for IMERGF. Specifically, IMERGF and PUnet demonstrate the highest correlations (0.70 and 0.63, respectively), while PDIR shows the lowest (0.38). Regarding RMSE, which measures the overall deviation from the reference ST4, all four datasets display similar values. Relative bias, which represents each dataset's tendency to overestimate or underestimate precipitation, varies from 6% for PUnet to 41% for IMERGF. Overall, the scatter plot reveals that although IMERGF exhibits strong correlations with ST4, it also has higher bias values. PDIR exhibits degraded performance, as evidenced by the large number of points that hug the X and Y axes in the scatter plot. In contrast, PUnet has a moderate correlation but lower bias and RMSE, demonstrating a more balanced performance in capturing precipitation patterns during the evaluation period. The unusual multi-modal structure in the PUnet scatterplot likely reflects regime-dependent behavior of the model during this case study. Training with the MSE loss function compresses extremes while tightening moderate values, and the subsequent quantile-mapping bias correction may further contribute to grouped patterns in scatter space.

d. Case study: Hurricane Idalia

Hurricane Idalia, a late-August 2023 tropical cyclone that struck the southeastern U.S., serves as a test case for assessing PUnet and other precipitation products during a high-impact rainfall event at hourly temporal resolution. Fig. 10 shows accumulated 6-hourly precipitation from hourly data during Hurricane Idalia (2023-08-30 00:00–06:00 UTC, 06:00–12:00 UTC, and 12:00–18:00 UTC) over the southeastern U.S., comparing HE, PDIR, PUnet, IMERGF, and the

reference ST4. All datasets capture the main precipitation core with lighter bands extending northeastward, though notable differences in spatial structure and intensity are evident. HE overestimates both the spread and intensity, producing overly dispersed rainfall patterns, while PDIR captures the high-intensity core but exaggerates extreme values. PUnet produces a compact, well-defined precipitation core that captures the general location and overall structure of the event; however, its precipitation field appears smoother than other products and does not fully reproduce the fine-scale variability evident in the ground-based reference ST4. IMERGF captures both the main core and surrounding bands well, maintaining strong similarity to ST4 in terms of peak location and intensity distribution. Across the three time steps, PUnet and IMERGF consistently track the temporal evolution of the event, whereas HE tends to smear precipitation, and PDIR overemphasizes extremes. Overall, IMERGF demonstrates the highest fidelity to the reference, followed by PDIR, which captures spatiotemporal patterns well, then PUnet, which preserves the core structure despite smoother fields, and HE, which performs comparatively weaker.

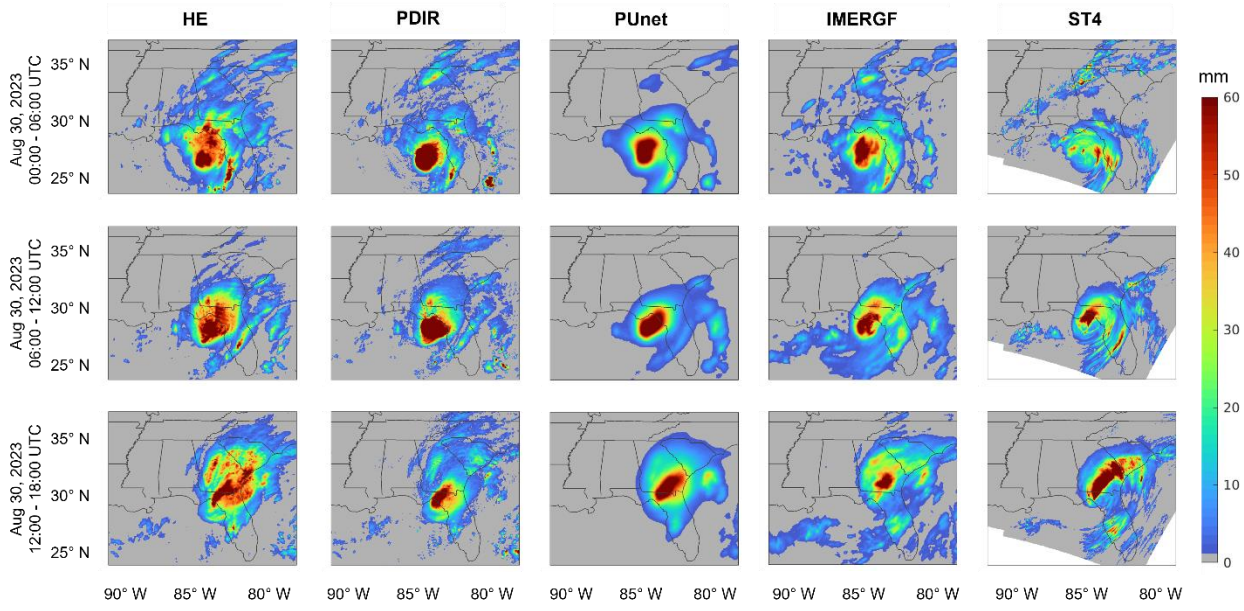


Fig. 10. Accumulated 6-hourly precipitation during Hurricane Idalia on 30 August 2023 (00:00–06:00 UTC, 06:00–12:00 UTC, and 12:00–18:00 UTC) over the southeastern US, comparing HE, PDIR, PUnet, and IMERGF against the reference ST4.

Taylor diagrams (Fig. 11) summarize the statistics of standard deviation, correlation, and centered root mean square deviation (RMSD) for the different hourly precipitation products across the three periods described above. In these diagrams, the radial axis represents the standard deviation of each dataset, the angular position (arc) indicates correlation with the ST4 reference, and the green dashed lines denote centered RMSD. PDIR consistently shows the weakest performance, with a standard deviation of ~16mm (about double the reference), low correlation of only ~0.44–0.48, and high centered RMSD. HE performs moderately, with a standard deviation of ~13-14mm and correlation of ~0.60–0.70, indicating improvement over PDIR but still an inflated variability relative to the reference. In contrast, PUnet and IMERG achieve the best agreement with ST4, with standard deviations closest to the reference, slightly higher correlations compared to HE, and positions nearest to the lower RMSD contours. Consistent with the bulk CONUS hourly analysis, these results confirm that PUnet and IMERG not only capture precipitation variability with magnitudes closer to the reference but also reproduce spatial–temporal patterns more accurately, whereas PDIR exhibits the highest variability and HE demonstrates intermediate performance.

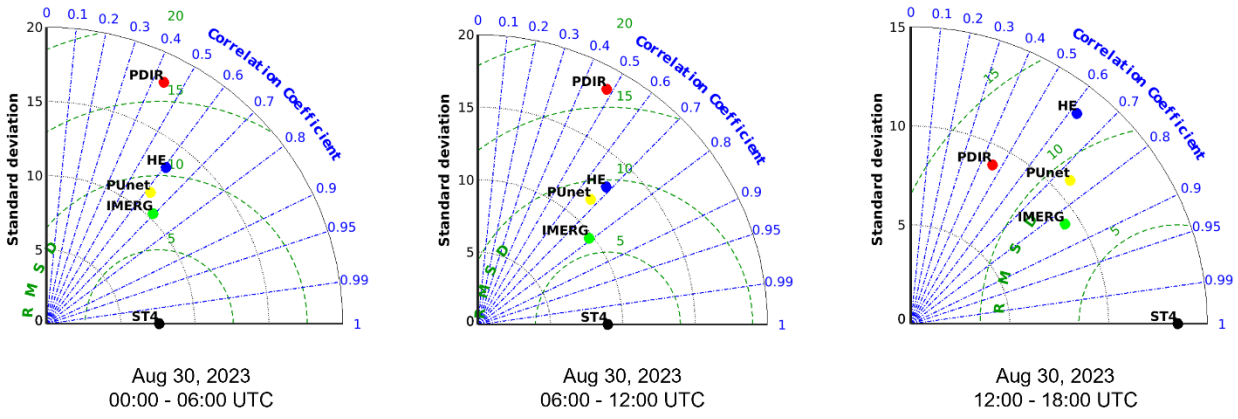


Fig. 11. Taylor diagrams summarizing the standard deviation, correlation, and centered root mean square deviation (RMSD) of hourly precipitation products (HE, PDIR, PUnet, and IMERGF) against ST4 across the three periods.

5. Conclusions

In this paper, we introduce PUnet, a novel satellite-based precipitation model that leverages deep learning with IR data to estimate global precipitation with short latency and low computational cost. The model avoids the need for image splitting and merging during processing, enhancing efficiency. However, because of the whole-image training approach, the current model may exhibit discontinuities at the dateline (180.0° line of longitude), which are mitigated by applying Gaussian smoothing and spatial blending as a post-processing step. Training at a coarser resolution and employing separate models for each of the 12 months allows the models to effectively capture seasonal variations in precipitation patterns and support consistent estimations throughout the year. It is also important to note that because IMERGF incorporates PDIR as its IR component and PUnet is trained on IMERGF, PUnet has an indirect connection to both models, so their global-scale comparison is not fully independent. Nonetheless, by leveraging information from IMERG (integrated PMW-IR-gauge precipitation) during training, PUnet provides a valuable alternative for near real-time estimation, weather prediction, and climate monitoring, especially when only infrared observations are available and short latency is crucial.

The global evaluation of precipitation estimation models highlights their varying capabilities in capturing precipitation patterns worldwide. Among the assessed datasets, PUnet demonstrates strong performance, ranking first in CORR against IMERGF and outperforming the other products in RMSE and MAE for mean global annual precipitation during 2022–2023. The meridional analysis shows that PUnet (and PDIR) align closely with IMERGF across all longitudes, demonstrating strong large-scale performance. Minor discrepancies, such as positive biases near 60°W (Amazon Basin) and negative biases around 70°E (western Indian Ocean), likely stem from the limited sensitivity of IR-based inputs to warm rain processes (Ombadi et al. 2021). In the zonal analysis, PUnet exhibits the best agreement with IMERGF across most latitudes, with only slight deviations near the equator—an area influenced by the ITCZ and other complex weather systems (Dezfuli 2017; Nicholson 2018). These findings highlight PUnet's robustness while acknowledging regional challenges in precipitation estimation.

Evaluation over CONUS highlights PUnet's performance relative to the established products HE, PDIR, and IMERGF, using ST4 as the reference for the period 2022–2023. While all of them tend to overestimate precipitation in the southeastern CONUS, PUnet demonstrates strong

correlation to ST4 and competitive performance despite some limitations, such as a higher RMSE compared to IMERGF. PUnet performs well in estimating precipitation along the West Coast, and while the coarser model output resolution inherently smooths precipitation, the UNet's convolutional operations may further contribute to the smoothing of accumulated precipitation patterns. The evaluation of extreme precipitation indices shows that PUnet aligns well with ST4 for the number of heavy precipitation days (R10mm), the maximum dry (CDD) and wet (CWD) spell duration. However, PUnet tends to overestimate the total precipitation from very extreme events (R95pTOT and R99pTOT), indicating a bias toward more extreme events and remaining room for improvement in balancing intensity and frequency estimates. Despite this, PUnet generally approximates ST4 more closely than HE and PDIR.

A case study of an extreme precipitation event over the Western U.S. on December 26-27, 2022, further highlights the strengths and limitations of the current model, using ST4 as the reference. PUnet, despite its lower resolution and smoother characteristics, effectively captures the overall precipitation pattern without the overestimation seen in IMERGF, which tends to overestimate precipitation in Southern California, Washington, and Montana. HE and PDIR, while accurate along the coast, similarly overestimate inland areas. Scatter plots of 6-hourly precipitation estimates against ST4 reveal varying levels of agreement among the datasets, with IMERGF showing the highest correlations but (again) higher bias values. In contrast, PUnet demonstrates a balanced performance with a moderate correlation, low bias, and RMSE, suggesting reduced systematic error and a closer approximation to the reference ST4. The Hurricane Idalia case study shows that PUnet accurately captures the spatial and temporal structure of extreme precipitation events. Compared to HE and PDIR, PUnet closely matches ST4 in intensity and variability at hourly resolution, with minor differences in light-rain areas. These results highlight PUnet as a high-fidelity IR-based product capable of reproducing extreme rainfall patterns with performance comparable to IMERGF.

This research aims to develop an operational global precipitation estimation model that delivers near-real-time results with high consistency whenever IR data is available, focusing on implementation at a global scale. By leveraging deep neural networks and advanced processing techniques, PUnet can train and operate on a complete global image, reducing processing time and computational cost while maintaining high accuracy across temporal and spatial scales. With

potential temporal coverage limited only by the availability of globally measured IR data—reliably retrieved since 1983 (Ashouri et al. 2015)—PUnet also offers significant potential for creating a high-resolution climate data record. Future efforts could refine PUnet by incorporating additional data sources and further optimizing its architecture to improve its accuracy in capturing extreme precipitation events. Integrating complementary data, such as PMW or radar observations, could mitigate biases and enhance performance in regions where IR data alone may fall short, while techniques like transfer learning could extend its applicability across diverse climatic zones (Huffman et al. 2007; Zhuang et al. 2020). Building on its strong foundation and this preliminary evaluation, researchers at CHRS are optimistic that PUnet will become the next product in the PERSIANN family, following PDIR-Now.

Acknowledgments.

This research was supported by NOAA Climate Program Office's Climate Observations and Monitoring Program under Grant NA23OAR4310443, NASA under Grants 80NSSC23K0136 and 80NSSC21K1668, the Center for Western Weather and Water Extremes (CW3E) at the Scripps Institution of Oceanography through the AR Program Grant 4600013361, sponsored by the California Department of Water Resources and the USACE FIRO III Grant W912HZ2420001. Additionally, this work was funded by NOAA through Grant ST133017CQ0058 with Riverside Technology, Inc. We also gratefully acknowledge the support from the NVIDIA Academic Hardware Grant Program. The computational resources were supported by Google Cloud through the Google Cloud Research Credits program.

Data Availability Statement.

Global near-real-time satellite precipitation data generated by the PERSIANN-Unet algorithm and demo are available through the CHRS Data Portal (https://chrsdata.eng.uci.edu/) and CHRS iRain (https://irain.eng.uci.edu).

All input and evaluation datasets used in this study are publicly available: NCEP Stage IV precipitation analysis (Du 2011; https://doi.org/10.5065/D6PG1QDD), CPC 4-km merged IR brightness temperature (Janowiak et al. 2017; https://doi.org/10.5067/P4HZB9N27EKU), GPM IMERG Final Run V07 (Huffman et al. 2023b; https://doi.org/10.5067/GPM/IMERG/3B-

775 HH/07), WorldClim2 precipitation climatology (Fick and Hijmans 2017;
776 https://doi.org/10.1002/joc.5086), HE (https://www.ospo.noaa.gov/products/atmosphere/ghe/)
777 and PDIR-Now (Nguyen et al. 2020b; https://chrsdata.eng.uci.edu/). Full data citations
778 (including access dates where applicable) are provided in the References."

779 ## REFERENCES

780 AghaKouchak and N. Nakhjiri, "A near real-time satellite-based Global Drought Climate Data
781 record," Environmental Research Letters, vol. 7, no. 4, p. 044037, 2012.

782 Amell, A., Pfreundschuh, S., & Eriksson, P. (2024). The chalmers cloud ice climatology:
783 Retrieval implementation and validation. Atmospheric Measurement Techniques, 17(14),
784 4337-4368.

785 Ashouri, H., K. Hsu, S. Sorooshian, D. K. Braithwaite, K. R. Knapp, L. D. Cecil, B. R. Nelson,
786 and O. P. Prat, 2015: PERSIANN-CDR: Daily Precipitation Climate Data Record from
787 Multisatellite Observations for Hydrological and Climate Studies. Bull. Amer. Meteor. Soc.,
788 96, 69–83, https://doi.org/10.1175/BAMS-D-13-00068.1.

789 Ayzel, G., Heistermann, M., & Winterrath, T. (2019). Optical flow models as an open
790 benchmark for radar-based precipitation nowcasting (rainymotion v0. 1). Geoscientific
791 Model Development, 12(4), 1387-1402.

792 Beck, H. E., Pan, M., Roy, T., Weedon, G. P., Pappenberger, F., Van Dijk, A. I., ... & Wood, E.
793 F. (2019). Daily evaluation of 26 precipitation datasets using Stage-IV gauge-radar data for
794 the CONUS. Hydrology and Earth System Sciences, 23(1), 207-224.

795 Cannon, A. J., Sobie, S. R., & Murdock, T. Q. (2015). Bias Correction of GCM Precipitation by
796 Quantile Mapping: How Well Do Methods Preserve Changes in Quantiles and Extremes?.
797 Journal of Climate, 28(17), 6938-6959. https://doi.org/10.1175/JCLI-D-14-00754.1

798 Chang, L. T. C., Cheung, K. K., & MCaneney, J. (2013). Case study of TRMM satellite rainfall
799 estimation for landfalling tropical cyclones: Issues and challenges. Tropical Cyclone
800 Research and Review, 2(2), 109-123.

801 Chen et al 2020 paper title (by Haonan Chen): A Machine Learning System for Precipitation
802 Estimation Using Satellite and Ground Radar Network Observations.

Dezfuli, A. (2017). Climate of western and central equatorial Africa. In Oxford research encyclopedia of climate science.

Du, J. 2011. NCEP/EMC 4KM Gridded Data (GRIB) Stage IV Data. Version 1.0. UCAR/NCAR - Earth Observing Laboratory [Dataset]. Accessed 09 Aug 2024, https://doi.org/10.5065/D6PG1QDD

Enayati, M., Bozorg-Haddad, O., Bazrafshan, J., Hejabi, S., & Chu, X. (2021). Bias correction capabilities of quantile mapping methods for rainfall and temperature variables. Journal of Water and Climate Change, 12(2), 401-419.

Faridzad, M., Yang, T., Hsu, K., Sorooshian, S., & Xiao, C. (2018). Rainfall frequency analysis for ungauged regions using remotely sensed precipitation information. Journal of Hydrology, 563, 123–142. https://doi.org/10.1016/j.jhydrol.2018.05.071

Fick, S.E. and Hijmans, R.J. (2017) WorldClim 2: New 1-km Spatial Resolution Climate Surfaces for Global Land Areas. International Journal of Climatology, 37, 4302-4315, accessed 12 November 2024, https://doi.org/10.1002/joc.5086

Gorooh, V. A., Asanjan, A. A., Nguyen, P., Hsu, K., & Sorooshian, S. (2022). Deep Neural Network High Spatiotemporal Resolution Precipitation Estimation (Deep-STEP) Using Passive Microwave and Infrared Data. Journal of Hydrometeorology, 23(4), 597-617. https://doi.org/10.1175/JHM-D-21-0194.1

He, K., Sun, J., & Tang, X. (2012). Guided image filtering. IEEE transactions on pattern analysis and machine intelligence, 35(6), 1397-1409.

Hsu, K., X. Gao, S. Sorooshian, and H. V. Gupta, 1997: Precipitation estimation from remotely sensed information using artificial neural networks. J. Appl. Meteor., 36, 1176–1190, https://doi.org/ 10.1175/1520-0450(1997)036,1176:PEFRSI.2.0.CO;2.

Huffman, G. J., Bolvin, D. T., Braithwaite, D., Hsu, K.-L., Joyce, R. J., Kidd, C., Nelkin, E. J., Sorooshian, S., Stocker, E. F., Tan, J., Wolff, D. B., & Xie, P. (2020). Integrated multi-satellite retrievals for the Global Precipitation Measurement (GPM) mission (IMERG). Advances in Global Change Research, 343–353. https://doi.org/10.1007/978-3-030-24568-9_19

Huffman, G. J., Bolvin, D. T., Nelkin, E. J., Wolff, D. B., Adler, R. F., Gu, G., ... & Stocker, E. F. (2007). The TRMM multisatellite precipitation analysis (TMPA): Quasi-global, multiyear, combined-sensor precipitation estimates at fine scales. Journal of hydrometeorology, 8(1), 38-55.

Huffman, G., Bolvin, D., Joyce, R., Nelkin, E., Tan, J., Braithwaite, D., Hsu, K., Kelley, O., Nguyen, P., Sorooshian, S., Watters, D., West, J., and Xie, P. (2023a). NASA Global Precipitation Measurement (GPM) Integrated Multi-satellitE Retrievals for GPM (IMERG) Version 07. Algorithm Theoretical Basis Document (ATBD) Version 47.

Huffman, G.J., E.F. Stocker, D.T. Bolvin, E.J. Nelkin, Jackson Tan (2023b), GPM IMERG Final Precipitation L3 Half Hourly 0.1 degree x 0.1 degree V07, Greenbelt, MD, Goddard Earth Sciences Data and Information Services Center (GES DISC), accessed 10 December 2024, https://doi.org/10.5067/GPM/IMERG/3B-HH/07

Janowiak, J. E., R. J. Joyce, and Y. Yarosh, 2001: A real-time global half-hourly pixel-resolution infrared dataset and its applications. Bull. Amer. Meteor. Soc., 82, 205–218, https://doi.org/10.1175/ 1520-0477(2001)082,0205:ARTGHH.2.3.CO;2.

Janowiak, J. B. X. P. J., Joyce, B., & Xie, P. (2017). NCEP/CPC L3 Half Hourly 4km global (60S-60N) merged IR V1. Greenbelt, MD, Goddard Earth Sciences Data and Information Services Center, accessed 10 December 2024, https://doi.org/10.5067/P4HZB9N27EKU.

Ji, S., Wei, S., & Lu, M. (2018). Fully convolutional networks for multisource building extraction from an open aerial and satellite imagery data set. IEEE Transactions on geoscience and remote sensing, 57(1), 574-586.

Joyce, R. J., J. E. Janowiak, P. A. Arkin, and P. Xie, 2004: CMORPH: A method that produces global precipitation estimates from passive microwave and infrared data at high spatial and temporal resolution. J. Hydrometeor., 5, 487–503, https:// doi.org/10.1175/1525-7541(2004)005,0487:CAMTPG.2.0.CO;2.

Li, X., Sungmin, O., Wang, N., & Huang, Y. (2021). Evaluation of the GPM IMERG V06 products for light rain over Mainland China. Atmospheric Research, 253, 105510.

Lin, Y., & Mitchell, K. E. (2005, January). 1.2 the NCEP stage II/IV hourly precipitation analyses: Development and applications. In Proceedings of the 19th Conference Hydrology, American Meteorological Society, San Diego, CA, USA (Vol. 10).

Lu, Z., Long, B., Li, K., & Lu, F. (2018). Effective guided image filtering for contrast enhancement. IEEE Signal Processing Letters, 25(10), 1585-1589.

Maraun, D. (2013). Bias correction, quantile mapping, and downscaling: Revisiting the inflation issue. Journal of Climate, 26(6), 2137-2143.

Mehran, A., & AghaKouchak, A. (2014). Capabilities of satellite precipitation datasets to estimate heavy precipitation rates at different temporal accumulations. Hydrological Processes, 28(4), 2262-2270.

Miller, S. W., P. A. Arkin, and R. Joyce, 2001: A combined microwave/infrared rain rate algorithm. Int. J. Remote Sens., 22, 3285–3307, https://doi.org/10.1080/01431160152609155.

Nepal, B., Shrestha, D., Sharma, S., Shrestha, M. S., Aryal, D., & Shrestha, N. (2021). Assessment of GPM-Era Satellite Products' (IMERG and GSMaP) Ability to Detect Precipitation Extremes over Mountainous Country Nepal. Atmosphere, 12(2), 254. https://doi.org/10.3390/atmos12020254

Nguyen, P., Shearer, E. J., Tran, H., Ombadi, M., Hayatbini, N., Palacios, T., ... & Sorooshian, S. (2019). The CHRS Data Portal, an easily accessible public repository for PERSIANN global satellite precipitation data. Scientific data, 6(1), 1-10, accessed 14 October 2024, https://doi.org/10.1038/sdata.2018.296

Nguyen, P., Ombadi, M., Gorooh, V. A., Shearer, E. J., Sadeghi, M., Sorooshian, S., Hsu, K., Bolvin, D., & Ralph, M. F. (2020b). Persiann Dynamic Infrared–rain rate (PDIR-now): A near-real-time, Quasi-Global satellite precipitation dataset. Journal of Hydrometeorology, 21(12), 2893–2906, accessed 12 October 2024, https://doi.org/10.1175/jhm-d-20-0177.1

Nguyen, P., Ombadi, M., Sorooshian, S., Hsu, K., AghaKouchak, A., Braithwaite, D., ... & Thorstensen, A. R. (2018). The PERSIANN family of global satellite precipitation data: A

review and evaluation of products. Hydrology and Earth System Sciences, 22(11), 5801-5816.

Nguyen, P., Shearer, E. J., Ombadi, M., Gorooh, V. A., Hsu, K., Sorooshian, S., Logan, W. S., & Ralph, M. (2020a). PERSIANN Dynamic Infrared–Rain Rate Model (PDIR) for High-Resolution, Real-Time Satellite Precipitation Estimation. Bulletin of the American Meteorological Society, 101(3), E286-E302. https://doi.org/10.1175/BAMS-D-19-0118.1

Nicholson, S. E. (2018). The ITCZ and the Seasonal Cycle over Equatorial Africa. Bulletin of the American Meteorological Society, 99(2), 337-348. https://doi.org/10.1175/BAMS-D-16-0287.1

Ombadi, M., Nguyen, P., Sorooshian, S., & Hsu, K. L. (2021). How much information on precipitation is contained in satellite infrared imagery?. Atmospheric Research, 256, 105578.

Pan, B., Hsu, K., AghaKouchak, A., & Sorooshian, S. (2019). Improving precipitation estimation using Convolutional Neural Network. Water Resources Research, 55(3), 2301–2321. https://doi.org/10.1029/2018wr024090

Pfreundschuh, S., Ingemarsson, I., Eriksson, P., Vila, D. A., & Calheiros, A. J. (2022a). An improved near-real-time precipitation retrieval for Brazil. Atmospheric Measurement Techniques, 15(23), 6907-6933.

Pfreundschuh, S., Brown, P. J., Kummerow, C. D., Eriksson, P., & Norrestad, T. (2022b). GPROF-NN: A neural-network-based implementation of the Goddard profiling algorithm. Atmospheric Measurement Techniques, 15(17), 5033-5060.

Pfreundschuh, S., Arulraj, M., Behrangi, A., Bogerd, L., Calheiros, A. J. P., Casella, D., ... & Tan, J. (2025). A Benchmark Dataset for Satellite-Based Estimation and Detection of Rain. arXiv preprint arXiv:2509.08816.

Prakash, S., Mitra, A. K., AghaKouchak, A., Liu, Z., Norouzi, H., & Pai, D. S. (2018). A preliminary assessment of GPM-based multi-satellite precipitation estimates over a monsoon dominated region. Journal of Hydrology, 556, 865-876.

912 Ravuri, S., Lenc, K., Willson, M., Kangin, D., Lam, R., Mirowski, P., ... & Mohamed, S.
913 (2021). Skilful precipitation nowcasting using deep generative models of radar. Nature,
914 597(7878), 672-677.

915 Ronneberger, O., Fischer, P., & Brox, T. (2015). U-net: Convolutional networks for biomedical
916 image segmentation. In Medical image computing and computer-assisted intervention–
917 MICCAI 2015: 18th international conference, Munich, Germany, October 5-9, 2015,
918 proceedings, part III 18 (pp. 234-241). Springer International Publishing.

919 Rozante, J. R., & Rozante, G. (2024). IMERG V07B and V06B: A comparative study of
920 precipitation estimates across South America with a detailed evaluation of Brazilian rainfall
921 patterns. Remote Sensing, 16(24), 4722.

922 Sadeghi, M., Nguyen, P., Hsu, K., & Sorooshian, S. (2020). Improving near real-time
923 precipitation estimation using a U-net convolutional neural network and geographical
924 information. Environmental Modelling & Software, 134, 104856.
925 https://doi.org/10.1016/j.envsoft.2020.104856

926 Sarojini, P. A. Stott, and E. Black, "Detection and attribution of human influence on regional
927 precipitation," Nature Climate Change, vol. 6, no. 7, pp. 669–675, 2016.

928 Sanò, P., Panegrossi, G., Casella, D., Marra, A. C., D'Adderio, L. P., Rysman, J. F., & Dietrich,
929 S. (2018). The passive microwave neural network precipitation retrieval (PNPR) algorithm
930 for the CONICAL scanning Global Microwave Imager (GMI) radiometer. Remote Sensing,
931 10(7), 1122.

932 Seo, D. J., Breidenbach, J., Fulton, R., Miller, D., & O'Bannon, T. (2000). Real-time adjustment
933 of range-dependent biases in WSR-88D rainfall estimates due to nonuniform vertical profile
934 of reflectivity. Journal of Hydrometeorology, 1(3), 222-240.

935 Scofield, R. A., and R. J. Kuligowski, 2003: Status and outlook of operational satellite
936 precipitation algorithms for extreme-precipitation events. Mon. Wea. Rev., 18, 1037-1051.

937 Sha, Y., Gagne II, D. J., West, G., & Stull, R. (2020). Deep-Learning-Based Gridded
938 Downscaling of Surface Meteorological Variables in Complex Terrain. Part II: Daily

Precipitation. Journal of Applied Meteorology and Climatology, 59(12), 2075-2092. https://doi.org/10.1175/JAMC-D-20-0058.1

Sorooshian, S., K.-L. Hsu, X. Gao, H. V. Gupta, B. Imam, and D. Braithwaite, 2000: Evaluation of PERSIANN system satellite-based estimates of tropical rainfall. Bull. Amer. Meteor. Soc., 81, 2035–2046, https://doi.org/10.1175/1520-0477(2000) 081,2035:EOPSSE.2.3.CO;2.

Sun, Q., C. Miao, Q. Duan, H. Ashouri, S. Sorooshian, and K. Hsu, 2018: A review of global precipitation data sets: Data sources, estimation, and intercomparisons. Rev. Geophys., 56, 79–107, https://doi.org/10.1002/2017RG000574.

Xiong, J., G. Tang, and Y. Yang, 2025: Continental evaluation of GPM IMERG V07B precipitation on a sub-daily scale. Remote Sensing of Environment, 321, 114690.

Yang, S., Ling, F., Li, Y., & Luo, J. (2023). Improving Seasonal Prediction of Summer Precipitation in the Middle–Lower Reaches of the Yangtze River Using a TU-Net Deep Learning Approach. Artificial Intelligence for the Earth Systems, 2(2), 220078. https://doi.org/10.1175/AIES-D-22-0078.1

Zhang, J., Howard, K., Langston, C., Kaney, B., Qi, Y., Tang, L., Grams, H., Wang, Y., Cocks, S., Martinaitis, S., Arthur, A., Cooper, K., Brogden, J., & Kitzmiller, D. (2016). Multi-radar multi-sensor (MRMS) quantitative precipitation estimation: Initial operating capabilities. Bulletin of the American Meteorological Society, 97(4), 621–638. https://doi.org/10.1175/bams-d-14-00174.1

Zhuang, F., Qi, Z., Duan, K., Xi, D., Zhu, Y., Zhu, H., ... & He, Q. (2020). A comprehensive survey on transfer learning. Proceedings of the IEEE, 109(1), 43-76.